Geometric collision rates and trajectories of cloud droplets falling into a Burgers vortex

Reginald J. Hill
Cooperative Institute for Research in Environmental Sciences, University of Colorado, and NOAA/Environmental Technology Laboratory, 325 Broadway, Boulder, Colorado 80305-3328

(Received 31 August 2004; accepted 21 December 2004; published online 22 February 2005)

Droplet velocities, concentrations, and geometric collision rates are calculated for droplets falling into Burgers vortices as a step toward understanding the role of turbulence-induced collisions of cloud water droplets. The Burgers vortex is an often used model of vortices in high Reynolds number turbulence. Droplet radii considered are 10, 20, and 40 μm; those radii are relevant to warm rain initiation. A method of calculating the concentrations of droplets along their trajectories by means of differential geometry is derived and implemented. A generalization of the rate of geometrical collisions of inertial particles is derived; the formulation applies for any local vorticity and rate of strain, and the classic collision-rate formula is obtained in the process. The relative velocities of droplets of different radii and their spatial variation of concentration affects spatial variation of collision rate; greater variation exists for a stronger vortex. The physical effects included in the droplet equation of motion are inertia, gravity, viscous drag, pressure and shear stress, added mass, the history integral, and the lift force. The lift force requires calculation of droplet angular velocity, the equation for which contains rotational inertial and viscous drag. An initial condition is found that does not cause an impulse in the history integral. The important terms in the droplets' equations of motion are found such that simpler approximate equations can be used. It is found that the lift force is negligible, the history integral is not. For smaller droplets in regions of lower vorticity, the time derivative of the difference of slip velocity and gravitationally induced drift velocity may be neglected. The present study suggests that acceleration-induced coalescence is most significant for droplets that are entrained into or formed within an intensifying vortex as distinct from falling toward the vortex.
[DOI: 10.1063/1.1858191]

I. INTRODUCTION

Turbulence is an essential aspect of Earth's clouds. Turbulence affects collisions, coalescence, and preferential concentration of cloud droplets and local supersaturation.[1–6] A long-standing mystery[7] and topic of vigorous current research[3,6] is how liquid-water clouds evolve from an almost unimodal droplet size distribution with median size of about 10 μm radius to contain enough droplets of large enough size (say 40 μm radius) to initiate rain by gravitationally induced coalescence. The issue is that this can occur on a time scale of 10 min rather than hours (e.g., see Shaw's[3] Fig. 3). Many hypotheses have been suggested[8] and continue to be investigated.[3] Amongst the hypotheses are several distinct effects of turbulence, including small-scale intermittency and turbulent accelerations. Empirical evidence exists to support turbulence mechanisms; for example, Pobanz *et al.*[9] found that regions of clouds where large droplets form are associated with strong wind shear, and therefore with turbulence. Our interest in the possibility that turbulent accelerations induce droplet coalescence arose from our finding[10] that the pressure-gradient correlation (and hence also the fluid-particle acceleration correlation) increases with turbulence Reynolds number, whereas older theories that assumed joint Gaussian probability density functions of velocity predicted no such increase. Even at the modest Reynolds numbers of wind-tunnel experiments and direct numerical simulation (DNS) the fluid-particle acceleration correlation was three times that predicted by the older theories.[11] Accelerations in high Reynolds number turbulence are strong. A typical turbulence energy dissipation rate in moderate cumulus convection is 100 $\mathrm{cm}^2\,\mathrm{s}^{-3}$, such that the root mean square (rms) of the turbulence acceleration is about one-third that of gravity.[3,12] Experiments in which particles are tracked in turbulence have quantified the probability density of accelerations to show that extreme events are likely because the accelerations are highly intermittent; for example, accelerations 26 times the rms occur at the 10^{-6} probability level.[13,14] Because only about 1 in 10^6 droplets grows to precipitation size, the phenomenon of droplet coalescence is that of rare events; suggesting that the large turbulent accelerations that occur in a small fraction of the flow might induce droplet coalescence.

Several facts simplify the hydrodynamics of cloud droplet motion. The volume of liquid water in a cloud is of the order of 10^{-6} of the air's volume and the ratio of mass densities of water to air is about 10^3. Therefore, air turbulence is unaffected by the presence of cloud droplets (of course, turbulence is generated, in part, by buoyancy created by exchange of latent heat). Further, only binary collisions need be considered. The smallest spatial scale of air turbulence (Kolmogorov's microscale) is of order 1 mm, whereas the size of droplets being considered is of order 10^{-2} mm. Consequently, vorticity and strain rate are approximately homogeneous in the neighborhood of each droplet. The small size of cloud droplets, and the fact that the ratio of the dynamic viscosity of air to that of water is 1.2×10^{-2}, and the surface tension of water, allows the cloud droplets to be approximated by rigid spheres. For example, the effect of that viscosity ratio on the Saffman lift force as determined by Legendre and Magnaudet[15] is only 0.8%. The rigid sphere approximation is important because there are no analytic equations of motion in the time domain for finite droplet viscosity.[16] The air flow around each droplet is laminar (small droplet Reynolds number) such that the viscous drag is well approximated by the Stokes force. Although limited by the above simplifications, the formulation and calculation in this paper apply to fluids other than air and water.

Despite the above simplifications, the equations solved here numerically are complicated. To best understand the numerical results, it is prudent to consider a simplified flow that has often been used to model vortices in turbulence. That flow is the Burgers vortex in its inviscid limit such that there is only an azimuthal velocity around the vortex center (Stokes drag on the droplets is not neglected). The simplicity of the chosen flow allows clear interpretation of droplet motion and collision. Vortex tubes have been documented in many DNS studies.[17] The velocity profile of vortex tubes in laboratory turbulence has been shown to be close to that of a Burgers vortex, from which the radii, circulation velocity, and spatial distribution of vortex tubes were obtained.[18,19]

Section II states the equation of motion of droplets, its justification, and the dimensionless equations. The initial velocities and positions are described in Sec. III. Derivation of the equations for calculation of concentration along a droplet trajectory is given in Sec. IV. Derivation of the generalization of the geometrical collision rate is given in Sec. V. The two Burgers vortex flow cases, called "gentle" and "strong," are described in Sec. VI. Sections VII and VIII give the trajectories, velocities, concentrations, and geometric collision rates as calculated for the gentle and strong vortex cases, respectively. Approximations to the equations of motion that are valid for the present calculations are given in Sec. IX.

II. DYNAMICAL EQUATIONS AND NOTATION

The equation of droplet motion that we solve is

$$
\begin{aligned}
m_d\frac{d\mathbf{V}}{dt} &= (m_d-m_f)\mathbf{g} - 6\pi a\mu(\mathbf{V}-\mathbf{u}) + m_f\frac{D\mathbf{u}}{Dt} \\
&\quad - \frac{1}{2}m_f\left(\frac{d\mathbf{V}}{dt}-\frac{D\mathbf{u}}{Dt}\right) - 6a^2(\pi\mu\rho)^{1/2} \\
&\quad \times\int_{-\infty}^{t} dt'\left(\frac{d\mathbf{V}}{dt'}-\frac{D\mathbf{u}}{Dt'}\right)(t-t')^{-1/2} \\
&\quad + \pi a^3\rho\left(\Omega-\frac{\omega}{2}\right)\times(\mathbf{V}-\mathbf{u}). \qquad (1)
\end{aligned}
$$

Here, m_d is droplet mass; $\mathbf{V}$ is droplet velocity; t is time; a is droplet radius, and ρ is the mass density of air such that $m_f=(4\pi a^3/3)\rho$ is the mass of air having the same volume as the droplet; $\mathbf{g}$ is the gravitational acceleration vector; μ is the coefficient of air viscosity; $\mathbf{u}$ is air velocity; $\mathbf{\Omega}$ is droplet angular velocity vector; $\omega=\nabla\times\mathbf{u}$ is air vorticity which equals twice the air angular velocity; d/dt and D/Dt denote time derivatives following the motion of the droplet and following the air motion, respectively. Thus, $d\mathbf{V}/dt$ is droplet acceleration and $D\mathbf{u}/Dt$ is the air's acceleration. The terms on the right-hand side of (1) are gravity, viscous drag, pressure and shear stress, acceleration of displaced air (added mass), history integral, and the lift force of Rubinow and Keller.[20] The lift force is demonstrated to be negligible in subsequent calculations. Lift forces dependent on nonzero viscosity have been obtained for uniform shear by Saffman,[21] who finds the Rubinow and Keller lift at the next order in droplet radius. The estimate of the relative magnitude of the lift forces of Saffman versus Rubinow and Keller as given by McLaughlin[22] shows that the Saffman lift can dominate for the large values of shear at small scales in clouds, but McLaughlin also shows that the range of droplet Reynolds number R_d for which the Saffman-type lift formula is valid is unknown for those same cases. Michaelides[16] reviews progress on Saffman-type lift forces, but points out that the analytic expressions are presently of too limited generality to be included in the equation of motion. An exception may be the formulas for all components of the lift forces given by Miyazaki *et al.*[23] for stationary homogeneous flow, but use of those formulas would overwhelm computer resources. For the present, we confine the calculation to the lift force of Rubinow and Keller.

Auton *et al.*[24] clarify that, for the case of inviscid flow, the added mass term must involve $d\mathbf{V}/dt-D\mathbf{u}/Dt$ and not $d\mathbf{V}/dt-d\mathbf{u}/dt$. Magnaudet *et al.*[25] prove the concept of added mass for nonuniform viscous flows and that $D\mathbf{u}/Dt$, not $d\mathbf{u}/dt$, must appear. Mei *et al.*[26] use numerical solution to determine that the added mass force is the same at finite and vanishing Reynolds numbers. Thus, the result of Auton *et al.*[24] also applies to viscous flow. Both the added mass and history terms are two aspects of a single unified derivation (see Landau and Lifschitz[27] and Clift *et al.*[28]) such that it seems that $d\mathbf{V}/dt-D\mathbf{u}/Dt$ must also appear in the history term, although $d\mathbf{V}/dt-d\mathbf{u}/dt$ appears more often in the literature (e.g., Michaelides,[16] Armenio and Fiorotto,[29] etc.). To prove which is the correct history kernel requires quantifying the effects of the history integral for nonuniform flow (i.e., $\nabla\mathbf{u}\neq0$) because $(d\mathbf{V}/dt-D\mathbf{u}/Dt)-(d\mathbf{V}/dt-d\mathbf{u}/dt)=(\mathbf{V}-\mathbf{u})\cdot\nabla\mathbf{u}$ [see (4) below]. Recently, Candelier *et al.*[30] report experimental data for a flow in which $\nabla\mathbf{u}\neq0$ and comparison with calculations for which both $d\mathbf{V}/dt-D\mathbf{u}/Dt$ and $d\mathbf{V}/dt-d\mathbf{u}/dt$ were used in the history integral. The result is that use of $d\mathbf{V}/dt-D\mathbf{u}/Dt$ overestimates and $d\mathbf{V}/dt-d\mathbf{u}/dt$ underestimates the history force required to agree with the data. Candelier *et al.*[30] give qualitative arguments in favor of $d\mathbf{V}/dt-d\mathbf{u}/dt$. On the other hand, the history integrand transitions to a more rapid decay than $(t-t')^{-1/2}$, as discussed below, such that the calculation by Candelier *et al.*[30] is expected to overestimate the effect of the history force; that argument qualitatively favors $d\mathbf{V}/dt-D\mathbf{u}/Dt$. Magnaudet *et al.*[25] argue that $d\mathbf{V}/dt-d\mathbf{u}/dt$ is correct because a time dependence is caused in the history force for their steady flow if $d\mathbf{V}/dt-D\mathbf{u}/Dt$ is used. On the other hand, their argument involves the abrupt introduction of acceleration at an initial time t_0. The time dependence that they obtain is correct in comparison with problem 7 in Sec. 24 of Landau and Lifshitz[27] when uniform acceleration is abruptly introduced into the history integral.

Correction for nonuniform flow leads to Faxen terms. Because of (4) below, the arguments of Auton *et al.*[24] suggest revision of Faxen laws. That is why Faxen terms (which were included by Maxey and Riley[31]) are absent in (1). By the above reasoning, we obtained (1), which is the same equation as given by Crowe *et al.*[32] (who include no lift force) and who state its equivalence to the derivation of Maxey and Riley[31] on the basis of small Reynolds number; (1) is also given by Manton.[33]

The effect of an initial impulse in the history integrand requires an additional term in the equation of motion, as shown by Reeks and McKee.[34] The intention of the calculations in this paper is to avoid any initial impulse in the history integrand. Mei *et al.*[26] use numerical solutions to determine a modification to the long-time behavior of the history integrand for the case of finite droplet Reynolds number R_d, and Mei[35] discusses how the inclusion of higher-order Reynolds-number effects in the drag requires modification of the history integral as well. By retaining effects to order R_d^2, Lawrence and Mei[36] show that the history integral for impulsive motion decays as t^{-2} at long times, and that for reversed and halted motion the history integral decays as t^{-1}. Both cases have more rapid decay than the $t^{-1/2}$ decay implied by the history integral in (1). Mei and Lawrence[37] study cases for which the particle suddenly starts, stops, and increases or decreases its speed; they elucidate cases for which the history integral has an asymptotic decay as t^{-1}. Lovalenti and Brady[38] formulate the force on particles which is correct to order R_d^2, including the history integral; that force includes effects of changes in direction of particle motion. Kim *et al.*[39] determine a kernel for the history integral that matches numerical solutions of the Navier–Stokes equation for the case of straight-line particle motion (axisymmetric flow, uniform ambient flow field); their history kernel reduces to the form in (1) at short times and changes to the t^{-2} decay at long times. Such studies do not include effects of spatial derivatives of the ambient flow on the particle motion; those effects do appear in (1) and our solutions. The generalizations of the history integral by Lovalenti and Brady[38] as well as by Kim *et al.*[39] have kernels that are not simply functions of $t-\tau$; consequently, an efficient algorithm for calculation of the history integral is not possible.

Although computer algorithms are not a topic here, our calculation of the history integral requires about one-half of the total computation time. That seems to be an improvement relative to difficulties reviewed by Michaelides.[16]

Because the droplet angular velocity $\mathbf{\Omega}$ appears in (1), we require its equation, namely,[27]

$$I\frac{d\mathbf{\Omega}}{dt} = -8\pi a^3\mu\left(\mathbf{\Omega}-\frac{\omega}{2}\right), \tag{2}$$

where $I=2m_d a^2/5$ is the rotational inertia of the droplet. The equation of droplet position $\mathbf{x}$ is

$$\frac{d\mathbf{x}}{dt} = \mathbf{V}. \tag{3}$$

Above, the air-flow properties $\mathbf{u}$, $D\mathbf{u}/Dt$, and ω, are evaluated at the droplet position $\mathbf{x}$ as they would exist in the absence of the droplet.

The time rate of change following the motion of an air particle, D/Dt, is related to the time rate of change observed from a fixed reference frame $\partial/\partial t$ (Eulerian observer) by $D/Dt=(\partial/\partial t)+\mathbf{u}\cdot\nabla$, where ∇ is the spatial gradient operator. Likewise, for the time rate of change following a droplet, d/dt, the relationship is $d/dt=(\partial/\partial t)+\mathbf{V}\cdot\nabla$. The difference of these operators gives the obvious and useful result that

$$\frac{d}{dt} = \frac{D}{Dt} + (\mathbf{V}-\mathbf{u})\cdot\nabla. \tag{4}$$

In subsequent calculations, there are large cancellations between the terms $(m_d-m_f)\mathbf{g}$ and $-6\pi a\mu(\mathbf{V}-\mathbf{u})$ in (1), especially for small droplet radius. Those cancellations reduce useful computer word length. Therefore, we change the dependent variable from $\mathbf{V}$ to $\mathbf{w}$, as defined by

$$\mathbf{w} \equiv \mathbf{V}-\mathbf{u}-\mathbf{U}_d, \tag{5}$$

where

$$\mathbf{U}_d \equiv (m_d-m_f)\mathbf{g}/6\pi a\mu$$

is the drift velocity of the droplet in still air. The cancellation is removed because

$$(m_d-m_f)\mathbf{g} - 6\pi a\mu(\mathbf{V}-\mathbf{u}) = -6\pi a\mu\mathbf{w}. \tag{6}$$

The equation for $\mathbf{w}$ requires $d\mathbf{w}/dt$, which is expressed in terms of known air-motion quantities $D\mathbf{u}/Dt$ and $\nabla\mathbf{u}$ by use of (4) and (5) as follows:

$$\frac{d\mathbf{w}}{dt} = \frac{d(\mathbf{V}-\mathbf{u})}{dt} = \frac{d\mathbf{V}}{dt} - \left(\frac{D\mathbf{u}}{Dt} + (\mathbf{V}-\mathbf{u})\cdot\nabla\mathbf{u}\right)$$
$$= \frac{d\mathbf{V}}{dt} - \frac{D\mathbf{u}}{Dt} - (\mathbf{w}+\mathbf{U}_d)\cdot\nabla\mathbf{u}. \tag{7}$$

More so, $\mathbf{\Omega}$ and $\omega/2$ are so nearly equal in subsequent calculations that the computation of (2) would fail without the definition of the relative angular velocity of droplet and air, $\mathbf{S}$, as follows:

$$\mathbf{S} \equiv \mathbf{\Omega} - \frac{\omega}{2}. \tag{8}$$

Use of (4) and (8) gives

$$\frac{d\mathbf{S}}{dt} = \frac{d\mathbf{\Omega}}{dt} - \frac{1}{2}\frac{d\omega}{dt} = \frac{d\mathbf{\Omega}}{dt} - \frac{1}{2}\frac{D\omega}{Dt} - \frac{1}{2}(\mathbf{w}+\mathbf{U}_d)\cdot\nabla\omega.$$

The equations of motion are next expressed in dimensionless form. For that purpose, define the following parameters: $U_d=|\mathbf{U}_d|$ denotes the drift speed in still air; τ_d

$=m_d/6\pi a\mu$ is droplet relaxation time; $\ell_d=U_d\tau_d$ is droplet relaxation distance; $\hat{\mathbf{g}}=\mathbf{g}/g$ is the unit vector in the direction of gravity, and $g=|\mathbf{g}|$. The specific expression used here for droplet Reynolds number is $R_d=U_d a/\nu$, where $\nu=\mu/\rho$ is the kinematic viscosity. Add $(1/2)m_f d\mathbf{V}/dt$ to both sides of (1) and divide by $m_d+(1/2)m_f$. Scale all quantities by length and time scales ℓ_d and τ_d. That is, define $\tilde{t}\equiv t/\tau_d$ and $\tilde{t'}\equiv t'/\tau_d$, $\tilde{\mathbf{V}}\equiv\mathbf{V}/U_d$, $\tilde{\mathbf{u}}\equiv\mathbf{u}/U_d$, $\tilde{\mathbf{w}}\equiv\mathbf{w}/U_d$, $\tilde{\boldsymbol{\nabla}}\equiv\boldsymbol{\nabla}\ell_d$, $\tilde{\boldsymbol{\Omega}}\equiv\boldsymbol{\Omega}\tau_d$, $\tilde{\omega}\equiv\omega\tau_d$, $\tilde{\mathbf{S}}\equiv\mathbf{S}\tau_d$, and $\tilde{\mathbf{x}}\equiv\mathbf{x}/\ell_d$. Below, the tildes (i.e., ~) are deleted for clarity. Then (1) becomes the dimensionless equation

$$\frac{d\mathbf{w}}{dt}=-A\mathbf{w}-B\frac{D\mathbf{u}}{Dt}-(\mathbf{w}+\hat{\mathbf{g}})\cdot\boldsymbol{\nabla}\mathbf{u}-C\int_{-\infty}^{t}dt'\left(\frac{d\mathbf{w}}{dt'}+(\mathbf{w}+\hat{\mathbf{g}})\cdot\boldsymbol{\nabla}\mathbf{u}\right)(t-t')^{-1/2}-D\mathbf{S}\times(\mathbf{w}+\hat{\mathbf{g}}). \tag{9}$$

Here

$$A\equiv[1+(\gamma/2)]^{-1},\quad B\equiv(1-\gamma)A,\quad C\equiv(9\gamma/2\pi)^{1/2}A,\quad D\equiv(3\gamma/4)A,$$

where $\gamma\equiv m_f/m_d$. For water droplets in air, $\gamma\simeq10^{-3}$ so $A\simeq1$, $B\simeq1$, $C\simeq4\times10^{-2}$, and $D\simeq7\times10^{-4}$. The dependence of C on $\gamma^{1/2}$ shows that the history term becomes less important as γ decreases. Lawrence and Mei,[36] Vojir and Michaelides,[40] and Michaelides[16] point out that the history integral is of lesser importance when γ is small. Druzhinin and Ostrovsky[41] find that the history integral is significant for γ near unity; for their case $C\approx1$.

Written using our scaled variables, (2) becomes

$$\frac{d\mathbf{S}}{dt}=-\frac{1}{2}\frac{D\omega}{Dt}-\frac{1}{2}(\mathbf{w}+\hat{\mathbf{g}})\cdot\boldsymbol{\nabla}\omega-\frac{10}{3}\mathbf{S}, \tag{10}$$

and (3) becomes

$$\frac{d\mathbf{x}}{dt}=\mathbf{u}+\mathbf{w}+\hat{\mathbf{g}}. \tag{11}$$

Of course, all quantities in (9)–(11) are dimensionless.

III. INITIAL CONDITIONS

An important issue is how to start the droplet so as to not cause an impulse in the history integral. We found that an impulse strongly influences the subsequent calculation, in agreement with Reeks and McKee.[34] For example, if the droplet is initially moving with the air velocity, i.e., $\mathbf{V}=\mathbf{u}$ so $\mathbf{w}=-\mathbf{U}_d$, or if $\mathbf{w}=0$, then an impulse $d\mathbf{V}/dt-D\mathbf{u}/Dt$ is caused in the history integral. The initial condition $\mathbf{V}=\mathbf{u}$ has been used by Armenio and Fiorotto[29] to find that the history integral is significant for a very wide range of m_d/m_f, but the influence of the initial condition was not studied and the additional terms in the equation of motion required by Reeks and McKee[34] for an impulsive start were not included.

Various initial conditions were tried. The initial condition that the droplet is not spinning relative to the air is used, i.e., $\boldsymbol{\Omega}=\omega/2$ so $\mathbf{S}=0$. The history integral is assumed to be initially zero; in fact it is assumed to be zero throughout the prior unevaluated history from $t=-\infty$ to $t=t_0$, where t_0 is the initial time. This is a valid approximation if the droplets have been in quiescent flow prior to t_0. Our solutions of (9) showed that $d\mathbf{w}/dt$ evolves to become much smaller than the other terms in (9) when the air flow is not strong. Because the droplet initial positions are chosen to be where the flow is quiescent, the appropriate initial condition is $d\mathbf{w}/dt=0$. Substitution of $d\mathbf{w}/dt=0$ in (9) and moving terms that contain $\mathbf{w}$ to the left-hand side give, at $t=t_0$,

$$A\mathbf{w}+\mathbf{w}\cdot\boldsymbol{\nabla}\mathbf{u}=-B\frac{D\mathbf{u}}{Dt}-\hat{\mathbf{g}}\cdot\boldsymbol{\nabla}\mathbf{u}. \tag{12}$$

Since $D\mathbf{u}/Dt$ and $\boldsymbol{\nabla}\mathbf{u}$ are known at the initial position, (12) is an algebraic equation that is solved to obtain the initial $\mathbf{w}$.

IV. CONCENTRATIONS ALONG TRAJECTORIES

To calculate the rate of collisions of droplets of one radius with droplets of another radius at a given place in the flow, we must know the concentration of both types of droplets. The concentration along a droplet trajectory is relative to the concentration at the initial point on the trajectory $\mathbf{x}(t_0)$ at the initial time t_0. The concentrations can be determined by calculating a dense set of trajectories such that the local distance between trajectories can be calculated. Differential geometry offers a better method. Calculating both methods has verified the derivation and programming of the method from differential geometry. Consider one trajectory, $\mathbf{x}=\mathbf{x}[\mathbf{x}(t_0),t_0,t]$; it is the locus of points through which the center of a droplet passes. The meaning of the argument list $[\mathbf{x}(t_0),t_0,t]$ is as follows: a point $\mathbf{x}$ on the trajectory depends on the initial position of the droplet $\mathbf{x}(t_0)$; for unsteady flow, $\mathbf{x}$ depends explicitly on when the droplet was released (i.e., on t_0); $\mathbf{x}$ also depends on the duration since release, $t-t_0$, and therefore on t. The initial velocity for the trajectory $\mathbf{x}$ is $\mathbf{V}_0$, which is obtained from (12) and (5). The initial concentration of droplets is N_0. Of course, $\mathbf{V}_0$ and N_0 depend on $\mathbf{x}(t_0)$, and, for unsteady flow, $\mathbf{V}_0$ and N_0 depend explicitly on t_0 as well. One could prescribe a dependence of N_0 on t_0 even if $\mathbf{V}_0$ is constant, and vice versa. It is useful to think of the differential of time dt as being a constant time step used throughout the integration of the equations.

Let the initial points of trajectories of identical droplets lie in a plane that is normal to $\hat{\mathbf{g}}$. Let Cartesian coordinates in that plane be x_0,y_0. Consider an infinitesimal rectangle in the initial plane; differential displacements dx_0 and dy_0 are the lengths of the sides of the rectangle; the center of the rectangle is the initial point of the trajectory $\mathbf{x}(t_0)$. Consider the volume swept out by the continuum of trajectories that have their initial points in that infinitesimal rectangle. Between times t_0 and t_0+dt, those trajectories advance by the vector displacement $\mathbf{V}_0dt$, thereby forming a parallelepiped of height $\hat{\mathbf{g}}\cdot\mathbf{V}_0dt$ such that volume swept out in the first time step of duration dt is $dx_0dy_0\hat{\mathbf{g}}\cdot\mathbf{V}_0dt$. Differential geometry gives us the fact that further along the trajectory $\mathbf{x}(t)$ at a later time t, the points on the initial infinitesimal rectangle form a surface of area $dx_0dy_0|\partial\mathbf{x}/\partial x_0\times\partial\mathbf{x}/\partial y_0|$ having unit normal $(\partial\mathbf{x}/\partial x_0\times\partial\mathbf{x}/\partial y_0)/|\partial\mathbf{x}/\partial x_0\times\partial\mathbf{x}/\partial y_0|$. The partial derivatives $\partial\mathbf{x}/\partial x_0$ and $\partial\mathbf{x}/\partial y_0$ are the changes in the trajectory's position at time t for a given infinitesimal change in the initial point of the trajectory. In the differential of time dt, this surface advances by the vector displacement $\mathbf{V}(\mathbf{x},t)dt$ thereby sweeping out a volume $dx_0 dy_0(\partial\mathbf{x}/\partial x_0 \times \partial\mathbf{x}/\partial y_0)\cdot\mathbf{V}(\mathbf{x},t)dt$. For equal differentials dt, the same points swept out the initial differential volume as swept out the later one. The number of points in each volume is the concentration along the trajectory $N(\mathbf{x},t)$ multiplied by the volume. That is, equating the number of points gives $dx_0\, dy_0(\partial\mathbf{x}/\partial x_0\times\partial\mathbf{x}/\partial y_0)\cdot\mathbf{V}(\mathbf{x},t)dtN(\mathbf{x},t)=dx_0dy_0\hat{\mathbf{g}}\cdot\mathbf{V}_0 dtN_0$, from which is obtained the ratio of the concentration along the trajectory to the initial concentration:

$$N(\mathbf{x},t)N_0 = \hat{\mathbf{g}}\cdot\mathbf{V}_0 \Bigg/ \left(\frac{\partial\mathbf{x}}{\partial x_0}\times\frac{\partial\mathbf{x}}{\partial y_0}\right)\cdot\mathbf{V}(\mathbf{x},t). \tag{13}$$

Because $\mathbf{x}=\mathbf{x}[\mathbf{x}(t_0),t_0,t]$, the argument list of $N(\mathbf{x},t)$ and $\mathbf{V}(\mathbf{x},t)$ can also be written as $[\mathbf{x}(t_0),t_0,t]$, where the explicit dependence on t_0 is for the case of unsteady flow. One can consider unsteady initial conditions in the sense that one can allow t_0 to increase and start new droplets at the initial plane as t_0 increases; for each droplet, t begins at that droplet's t_0 and thereafter increases. The problem of determining the concentration of droplets, $N(\mathbf{x},t)$, is reduced to specifying N_0 and calculating the partial derivatives $\partial\mathbf{x}/\partial x_0$ and $\partial\mathbf{x}/\partial y_0$. The equations for those partial derivatives are given in the Appendix.

V. GEOMETRICAL COLLISION RATES

A. The classic collision mechanism

The problem of calculating geometric collision rates of spheres was studied over a century ago by Boltzmann[42] (modern texts such as Harr's[43] are easier to read). The concentration is assumed to be so small that only binary collisions are considered; this is accurate for applications to clouds. Let subscripts 1 and 2 denote two droplets whose collision is under consideration at point $\mathbf{x}$ and time t. Their radii are a_1 and a_2. The droplets touch at one point when the separation vector from the center of droplet 1 to the center of droplet 2, namely $\mathbf{R}=\mathbf{x}_2-\mathbf{x}_1$, has magnitude a_1+a_2. The relative velocity of the droplets when $|\mathbf{R}|=a_1+a_2$ is denoted by $\mathbf{V}_R(\mathbf{x},t)=\mathbf{V}_2(\mathbf{x}_2,t)-\mathbf{V}_1(\mathbf{x}_1,t)$; the meaning of the argument list $(\mathbf{x},t)$ is that, within the present approximation, $\mathbf{V}_2$ and $\mathbf{V}_1$ are nearly constant within distances of order a_1+a_2 from $\mathbf{x}_2$ and $\mathbf{x}_1$, respectively. The concentrations $N_1(\mathbf{x}_1,t)$ and $N_2(\mathbf{x}_2,t)$ are approximated by $N_1(\mathbf{x},t)$ and $N_2(\mathbf{x},t)$. One collision is counted when the droplets' surfaces touch at one point and the distance between their centers is decreasing (i.e., $\mathbf{R}\cdot\mathbf{V}_R$ is negative). If the radii a_1 and a_2 are equal, or nearly so, then there is the possibility that their trajectories are nearly parallel, and $\mathbf{V}_R$ nearly vanishes; then the mechanism of collision is the crowding together of adjacent trajectories. In this case, $\mathbf{V}_R$ can depend on the direction of $\mathbf{R}$; then the classic formula for collision rate does not apply. That case is considered in Sec. V B. For distinctly different radii, $\mathbf{V}_R$ is substantial because $\mathbf{V}_2$ and $\mathbf{V}_1$ differ in direction or magnitude or both. For this case, $\mathbf{V}_R$ is constant on the spatial scale of order a_1+a_2 surrounding the given droplets; this simplifies the integration of collision rate over the direction of $\mathbf{R}$ such that the classic formula applies. The classic formula for the number of collisions of droplets 1 and 2 at a given location $\mathbf{x}$ per unit volume per unit time is $\pi N_1 N_2|\mathbf{R}|^2|\mathbf{V}_R|$. From (13), the concentrations are known relative to the initial concentrations N_{01} and N_{02} that exist at the beginning of their respective trajectories. Let $\sigma(\mathbf{x},t)$ denote the number of collisions of droplets of type 1 and 2 per unit volume per unit time per unit initial concentration N_{01} and per unit initial concentration N_{02}; the classic formula is

$$\sigma(\mathbf{x},t) = \pi\frac{N_1(\mathbf{x},t)}{N_{01}}\frac{N_2(\mathbf{x},t)}{N_{02}}(a_1+a_2)^2|\mathbf{V}_R(\mathbf{x},t)|. \tag{14}$$

It is understood that (14) applies where each type of droplet has a trajectory.

B. Generalized collision formula

Now consider the generalization of (14) to include the case of equal-size droplets, or nearly equal-size droplets. For that case, one can visualize the geometric collision rate as being caused by the crowding together of trajectories. The classic theory[42,43] for the number of collisions of droplets of type 1 and 2 per unit volume per unit time while the unit vector $\hat{\mathbf{R}}\equiv\mathbf{R}/(a_1+a_2)$ points within the differential of solid angle $d\Omega_{\hat{\mathbf{R}}}$ is

$$N_1(\mathbf{x}_1)N_2(\mathbf{x}_2)(a_1+a_2)^2\hat{\mathbf{R}}\cdot[\mathbf{V}_2(\mathbf{x}_2)-\mathbf{V}_1(\mathbf{x}_1)]d\Omega_{\hat{\mathbf{R}}}, \tag{15}$$

where the dependence on t has been suppressed for brevity. Define the centroid position $\mathbf{C}=(\mathbf{x}_2+\mathbf{x}_1)/2$. Taylor's series gives

$$\mathbf{V}_2(\mathbf{x}_2) = \mathbf{V}_2(\mathbf{C}) + (\mathbf{x}_2-\mathbf{C})\cdot[\nabla_{\mathbf{x}}\mathbf{V}_2(\mathbf{x})]_{\mathbf{x}=\mathbf{C}}+\cdots$$

and a similar series for $\mathbf{V}_1(\mathbf{x}_1)$. Noting that $\mathbf{x}_2-\mathbf{C}=\mathbf{R}/2$ and $\mathbf{x}_1-\mathbf{C}=-\mathbf{R}/2$, the difference of the two series gives

$$\mathbf{V}_2(\mathbf{x}_2)-\mathbf{V}_1(\mathbf{x}_1) = [\mathbf{V}_2(\mathbf{C})-\mathbf{V}_1(\mathbf{C})]+\frac{\mathbf{R}}{2}\cdot\{\nabla_{\mathbf{x}}[\mathbf{V}_2(\mathbf{x}) + \mathbf{V}_1(\mathbf{x})]\}_{\mathbf{x}=\mathbf{C}}+\cdots.$$

The first two terms of this series suffice on the spatial scale of order a_1+a_2 surrounding the given droplets. Substitution of the first two terms of this series into (15) gives two terms

$$N_1(\mathbf{x}_1)N_2(\mathbf{x}_2)(a_1+a_2)^2\hat{\mathbf{R}}\cdot[\mathbf{V}_2(\mathbf{C})-\mathbf{V}_1(\mathbf{C})]d\Omega_{\hat{\mathbf{R}}}, \tag{16}$$

$$N_1(\mathbf{x}_1)N_2(\mathbf{x}_2)(a_1+a_2)^3 \times\hat{\mathbf{R}}\cdot\left[\left(\hat{\mathbf{R}}\cdot\nabla_{\mathbf{x}}\right)\frac{\mathbf{V}_2(\mathbf{x})+\mathbf{V}_1(\mathbf{x})}{2}\right]_{\mathbf{x}=\mathbf{C}}d\Omega_{\hat{\mathbf{R}}}. \tag{17}$$

One could also introduce series expansions for $N_1(\mathbf{x}_1)$ and $N_2(\mathbf{x}_2)$ to find yet more terms arising from the gradients of N_1 and N_2.

The first term (16) leads to (14) as follows. Now, $\hat{\mathbf{R}}\cdot[\mathbf{V}_2(\mathbf{C})-\mathbf{V}_1(\mathbf{C})]=|\mathbf{V}_2(\mathbf{C})-\mathbf{V}_1(\mathbf{C})|\cos\theta$, which defines the polar angle θ of a spherical coordinate system; let ϕ denote the azimuthal angle. Integrate (16) over all solid angles for which $\cos\theta$ is positive; this corresponds to the distance between the droplets decreasing when their surfaces touch at one point. Thus, θ varies from 0 to $\pi/2$ and ϕ varies from 0 to 2π, and the integrand is $\cos\theta\sin\theta$. The integration produces $\pi N_1(\mathbf{x}_1)N_2(\mathbf{x}_2)(a_1+a_2)^2|\mathbf{V}_2(\mathbf{C})-\mathbf{V}_1(\mathbf{C})|$; when this is normalized by the initial concentrations and the distinction between $N_2(\mathbf{x}_2)$ and $N_2(\mathbf{x}_1)$ is neglected, then we recover (14).

The contribution of the second term (17) to the collision rate is determined as follows. Index notation is more convenient in the second term (17), within which we have

$$\hat{\mathbf{R}} \cdot \{(\hat{\mathbf{R}} \cdot \boldsymbol{\nabla}_{\mathbf{x}})[\mathbf{V}_2(\mathbf{x}) + \mathbf{V}_1(\mathbf{x})]/2\} = \hat{R}_i\hat{R}_j[\partial(V_{2_j} + V_{1_j})/\partial x_i]/2 = \hat{R}_i\hat{R}_j s_{ij}^{(V)}, \tag{18}$$

where

$$s_{ij}^{(V)} \equiv [(\partial V_{2_j}/\partial x_i + \partial V_{2_i}/\partial x_j)/2 + (\partial V_{1_j}/\partial x_i + \partial V_{1_i}/\partial x_j)/2]/2 = s_{ij}^{(w)} + s_{ij}^{(u)}, \tag{19}$$

where $s_{ij}^{(u)} \equiv (\partial u_j/\partial x_i + \partial u_i/\partial x_j)/2$ is the strain rate of the air flow and $s_{ij}^{(w)} \equiv [(\partial w_{2_j}/\partial x_i + \partial w_{2_i}/\partial x_j)/2 + (\partial w_{1_j}/\partial x_i + \partial w_{1_i}/\partial x_j)/2]/2$. Integration of (18) over solid angles gives the following integral:

$$I \equiv \int\int \hat{R}_i\hat{R}_j s_{ij}^{(V)} \sin\theta \, d\theta \, d\phi, \tag{20}$$

where the integration is over only the portion of the unit sphere where $\hat{R}_i\hat{R}_j s_{ij}^{(V)} < 0$, which corresponds to approaching droplets. In an EPAPS document,[44] the computational algorithms for (19) and (20) are discussed, as is reduction of the double integral in (20) to obtain a single integral that can be tabulated. Now, the contribution of (17) to the number of collisions of droplets of type 1 and 2 per unit volume per unit time per unit of both initial concentrations is

$$\frac{N_1(\mathbf{x},t)}{N_{01}}\frac{N_2(\mathbf{x},t)}{N_{02}}(a_1 + a_2)^3|I|. \tag{21}$$

At this point the distinctions between $N_1(\mathbf{x})$ and $N_1(\mathbf{x}_1)$, $N_2(\mathbf{x})$ and $N_2(\mathbf{x}_2)$, $\mathbf{V}_1(\mathbf{C})$ and $\mathbf{V}_1(\mathbf{x}_1)$, and $\mathbf{V}_2(\mathbf{C})$ and $\mathbf{V}_2(\mathbf{x}_2)$ are neglected; for instance, the Taylor series would not be convergent on scale a_1+a_2 if a singular point of the velocity fields were in the neighborhood of the collision point. The sum of (14) and (21) is the total collision rate.

The derivation of collision rate for small, inertialess particles by Mei and Hu[45] is a special case (i.e., for $\boldsymbol{\nabla} \cdot w = 0$) of the derivation above. Because (21) was obtained independently of their derivation and numerical validation, their result corroborates the present result. The collision rate above is a local and instantaneous value. The collision rate models of Sundaram and Collins[46] and of Wang *et al.*[47] are for volume and time averaged rates.

Saffman and Turner[48] considered, in their Secs. III and IV, the geometric collision rate caused by spheres moving with the air in a uniform strain-rate flow, in particular, their vorticity was zero. Their result is equivalent to use of $s_{ij}^{(V)} = s_{ij}^{(u)}$ to calculate (21). Our term $s_{ij}^{(w)}$ in (19) accounts for droplet motion relative to the flow. Although air-velocity derivatives enter (19) only in terms of the strain rate $s_{ij}^{(u)}$, we did not assume that the vorticity is zero. Also, Saffman and Turner[48] neglected (14), whereas our derivation obtains it.

VI. BURGERS VORTEX

Of the vortices used to model the small-scale structure of turbulence (Pullin and Saffman[17]), Burgers vortex[49] is the most common.[50] Burgers vortex is a steady, axially symmetric solution of the Navier–Stokes equation in which vorticity is maintained against viscous dissipation by an inward radial flow and outward axial flow. If only gravity and viscous drag are included on the right-hand side of (1), then there are multiple equilibrium points in the droplet's motion for a Burgers vortex.[51] The full equation (1) would produce yet more complex droplet motion. To best understand results from the complicated set of equations above, it is prudent to consider a simplified version of the Burgers vortex. To simplify the Burgers vortex, we consider its inviscid limit such that the radial and axial flows vanish (of course, Stokes drag on the droplets is not neglected). The flow is a vortex tube with a horizontal axis, i.e., transverse to gravity; call the axial direction as the z axis. The flow is two dimensional in the x-y plane. The simplicity of the chosen flow allows clear interpretation of droplet motion and collision. The vorticity is

$$\omega_z = \omega_0 e^{-(r/r_0)^2}. \tag{22}$$

The other vorticity components are zero. Thus, ω_0 is the vorticity at the center of the vortex; r is the distance from the center; r_0 is the parameter describing the size of the vortex. The azimuthal component of velocity calculated from $\omega = \boldsymbol{\nabla} \times \mathbf{u}$ is

$$u_\varphi = -\omega_0(r_0^2/2r)[1 - e^{-(r/r_0)^2}]. \tag{23}$$

The other velocity components are zero. Flow properties that appear in the equations to be solved that must be calculated are

$$\mathbf{u}, \quad \boldsymbol{\nabla}\mathbf{u}, \quad \boldsymbol{\nabla}\boldsymbol{\nabla}\mathbf{u}, \quad \frac{D\mathbf{u}}{Dt}, \quad \boldsymbol{\nabla}\frac{D\mathbf{u}}{Dt}, \quad \omega, \quad \boldsymbol{\nabla}\omega, \quad \boldsymbol{\nabla}\boldsymbol{\nabla}\omega, \quad \frac{D\omega}{Dt}, \quad \boldsymbol{\nabla}\frac{D\omega}{Dt}. \tag{24}$$

In accordance with (A1) in the Appendix, $\boldsymbol{\nabla}$ appears in (24) where $\partial/\partial x_0$ appears in the equations. Note that $\boldsymbol{\nabla}\boldsymbol{\nabla}\mathbf{u}$ and $\boldsymbol{\nabla}\boldsymbol{\nabla}\omega$ are third-order tensors. The air moves in circles around the vortex center such that, when following the motion of an air particle, the vorticity is constant; that is,

$$\frac{D\omega}{Dt} = 0, \quad \text{so} \quad \boldsymbol{\nabla}\frac{D\omega}{Dt} = 0.$$

Now, ω, $\boldsymbol{\nabla}\omega$, and $\boldsymbol{\nabla}\boldsymbol{\nabla}\omega$ are readily calculated from (22), as are $\mathbf{u}$, $\boldsymbol{\nabla}\mathbf{u}$, and $\boldsymbol{\nabla}\boldsymbol{\nabla}\mathbf{u}$ from (23). The contraction of the strain rate with itself is obtained from $\boldsymbol{\nabla}\mathbf{u}$; it is

$$s^2 \equiv s_{ij}^{(u)}s_{ij}^{(u)} = \frac{1}{2}\omega_0^2\left[e^{-(r/r_0)^2} - \left(\frac{r_0}{r}\right)^2(1 - e^{-(r/r_0)^2})\right]^2. \tag{25}$$

By comparison, Eq. (11) of Pumir[50] for s^2 is missing the rightmost exponent 2, which results from a misprint because

TABLE I. Flow parameters: left to right, maximum vorticity, vortex radius, maximum azimuthal speed, and Froude number. Gentle vortex, second row; strong vortex, bottom row.

ω_0 (s^{-1})	r_0 (cm)	U (cm s^{-1})	$11U^3/\Gamma g$
18	1	5.7	0.036
180	1/3	19	1.2

TABLE II. Droplet parameters: left to right, radius, drift speed, relaxation time, Reynolds number $R_d \equiv U_d a/\nu$.

a (μm)	U_d (cm s^{-1})	τ_d (s)	R_d
40	20	2.1×10^{-2}	4.2×10^{-1}
20	5.0	5.2×10^{-3}	5.3×10^{-2}
10	1.3	1.3×10^{-3}	6.8×10^{-3}

Fig. 12 of Pumir agrees with (25). Let p be pressure divided by air density. Poisson's equation is $\nabla^2 p=(\omega_y^2/2)-s^2$; after substituting (22) and (25), Poisson's equation is solved for the pressure gradient ∇p. Only the radial component of the pressure gradient is nonzero; it is given by

$$\frac{\partial p}{\partial r}=\frac{\omega_0^2 r_0^4}{4r^3}\left(1-e^{-(r/r_0)^2}\right)^2. \tag{26}$$

A further integration produces the same radial variation of pressure as is given in Eq. (12) of Pumir[50] that serves as a check of the calculation. For our inviscid case, the Navier–Stokes equation is $D\mathbf{u}/Dt=-\nabla p$, which determines $D\mathbf{u}/Dt$ from (26); $\nabla D\mathbf{u}/Dt$ in (24) is obtained by one further spatial differentiation. Now all quantities in (24) have been determined.

In high Reynolds number turbulence, the viscous force around strong vortex tubes is much less than the pressure-gradient force.[12] The inviscid Burgers vortex is a useful, simple model.

A. Calculated flow and droplet parameters

With the Burgers vortex as a model, one can determine Froude and Stokes numbers similar to those defined by Davila and Hunt.[52] Burgers[49] gives the circulation as $\Gamma=\pi\omega_0 r_0^2$; from (23) the maximum air speed is $U=0.32\omega_0 r_0$ at $r=1.1r_0$ and the maximum of $\partial u_\varphi/\partial r$ is $(\partial u_\varphi/\partial r)_{\max}=0.11\omega_0$ at $r=1.8r_0$; and from (26) the maximum of $\partial p/\partial r$ is $(\partial p/\partial r)_{\max}=0.11\omega_0^2 r_0$ at $r=0.74r_0$. Restoring the tilde notation (e.g., $\tilde{\mathbf{u}}$) to explicitly denote dimensionless quantities, the term $-BD\tilde{\mathbf{u}}/D\tilde{t}$ in (9) can be written as

$$-BD\tilde{\mathbf{u}}/D\tilde{t}=[1+(\gamma/2)]^{-1}(0.11\omega_0^2 r_0/g)\times[(D\mathbf{u}/Dt)/(\partial p/\partial r)_{\max}],$$

where the air acceleration is now scaled by its maximum $(\partial p/\partial r)_{\max}$. The factor $0.11\omega_0^2 r_0/g=1.1U^2/r_0 g=11U^3/\Gamma g$ is a Froude number (see Davila and Hunt[52]). For several Froude numbers, Marcu *et al.*[53] compute trajectories in counterrotating vortices using Stokes drag and gravity as the forces. If the rms acceleration in a cumulus cloud is of order $g/3$ as suggested in the Introduction, then, using the probability density of LaPorta *et al.*,[13] the probability of observing an acceleration equal to $0.11\omega_0^2 r_0$ is about unity for the gentle vortex and greater than 10^{-2} for the violent vortex. Despite relatively high probability, it is shown that the smaller droplets are deflected away from the position where $\partial p/\partial r$ is maximum. This has important implications where coalescence is prevalent.

Similarly, the third and fourth terms on the left-hand side of (9) contain the second-order tensor $\tilde{\nabla}\tilde{\mathbf{u}}$, which can be rescaled by the maximum of $\partial u_\varphi/\partial r$ such that $\tilde{\nabla}\tilde{\mathbf{u}}=0.11\omega_0\tau_d[\nabla\mathbf{u}/(\partial u_\varphi/\partial r)_{\max}]$. The coefficient $0.11\omega_0\tau_d=3.4\tau_d U^2/\Gamma$ is a Stokes number (see Davila and Hunt[52]).

A relatively gentle vortex having maximum air speed U of the order of the drift velocity U_d is chosen for the first calculation. A relatively strong vortex is chosen for the second calculation; its vorticity ω_0 is ten times that of the gentle vortex and its radius r_0 is smaller by a factor of 1/3. The flow parameters, including the Froude number $11U^3/\Gamma g$ are given in Table I. Consider cloud height of 3.1 km above mean sea level and temperature of 275 K; these values determine the viscosity of the air ($\nu=0.19$ cm^2 s^{-1}). As mentioned in the Introduction, a typical mean energy dissipation rate of cumulus clouds is 100 cm^2 s^{-3}, for which value the Kolmogorov microscale is $\eta=0.1$ cm. If r_0 is roughly 1 cm, then the position of the maximum of the pressure gradient from (26), i.e., $r=0.74r_0$, corresponds to the length scale of the pressure gradient correlation at high Reynolds numbers (about 5η, see Fig. 1 of Hill[54]). Therefore, $r_0=1$ cm is chosen for the gentle vortex. Table II gives the droplet drift velocity, relaxation time, and Reynolds number, $R_d\equiv U_d a/\nu$, for droplet radii of 40, 20, and 10 μm. Numerically calculated history-force kernels of Lawrence and Mei[36] differ from the formula of Mei and Adrian.[55] Nevertheless, a subjective estimate of the time of transition between the $t^{-1/2}$ decay at short times of the history integrand and the long-time decay can be obtained by equating the $t^{-1/2}$ and t^{-2} asymptotes in the formula of Mei and Adrian.[55] Using values from Table II for velocity U_d and Reynolds number $2R_d$ for equating those two asymptotes gives the times of transition to be roughly $10^{-2}\tau_d$, τ_d, and $50\tau_d$ for 40 μm, 20 μm, and 10 μm droplets, respectively. Thus, the history integral is overestimated in (1) for 40 μm droplets. From the value $R_d=0.42$, the drag is underestimated by the Stokes drag in (1) by about 15% for the 40 μm droplets, but is accurate for the smaller droplets.

A droplet remains motionless if it is brought to rest at an equilibrium point where the sum of all forces on it vanishes.

TABLE III. Stokes number and equilibrium positions. Gentle vortex: second and third columns. Strong vortex: fourth and fifth columns.

a (μm)	$3.4\tau_d U^2/\Gamma$	r_{equil}/r_0	$3.4\tau_d U^2/\Gamma$	r_{equil}/r_0
40	4.0×10^{-2}	None	4.0×10^{-1}	None
20	1.0×10^{-2}	0.71, 1.7	1.0×10^{-1}	0.17, 6.0
10	2.5×10^{-3}	0.15, 6.9	2.5×10^{-2}	0.043, 23

Neglecting the history integral, spin deflection, and initial conditions, one finds that, for the present flow, the equilibrium points are close to the horizontal axis that passes through the vortex center. To excellent approximation, the equilibrium points are on that axis at positions where the flow velocity is upward and equal to U_d. For $a=40$ μm, U_d exceeds the maximum air speed U of both the gentle and strong vortices (see Tables I and II) such that no equilibrium point exists. Our smaller droplets have two equilibrium points whose distances from the center of the vortex, r_{equil}/r_0, are given in Table III. The Stokes number discussed above, i.e., $3.4\tau_d U^2/\Gamma$, is also given in Table III.

VII. GENTLE VORTEX

A. Droplet trajectories and concentrations

Figure 1 shows trajectories of droplets of radius 10 μm which are falling from their initial points at the top of the figure. It is useful to think of the trajectories as potential trajectories that may be taken by droplets starting at random initial times and positions. On the top graph in Fig. 1, the speed of the droplets is indicated in color and a droplet's velocity vector is the unit tangent vector to the trajectory multiplied by the droplet speed. At the top of the top graph in Fig. 1, where the dominant forces are gravity and viscous

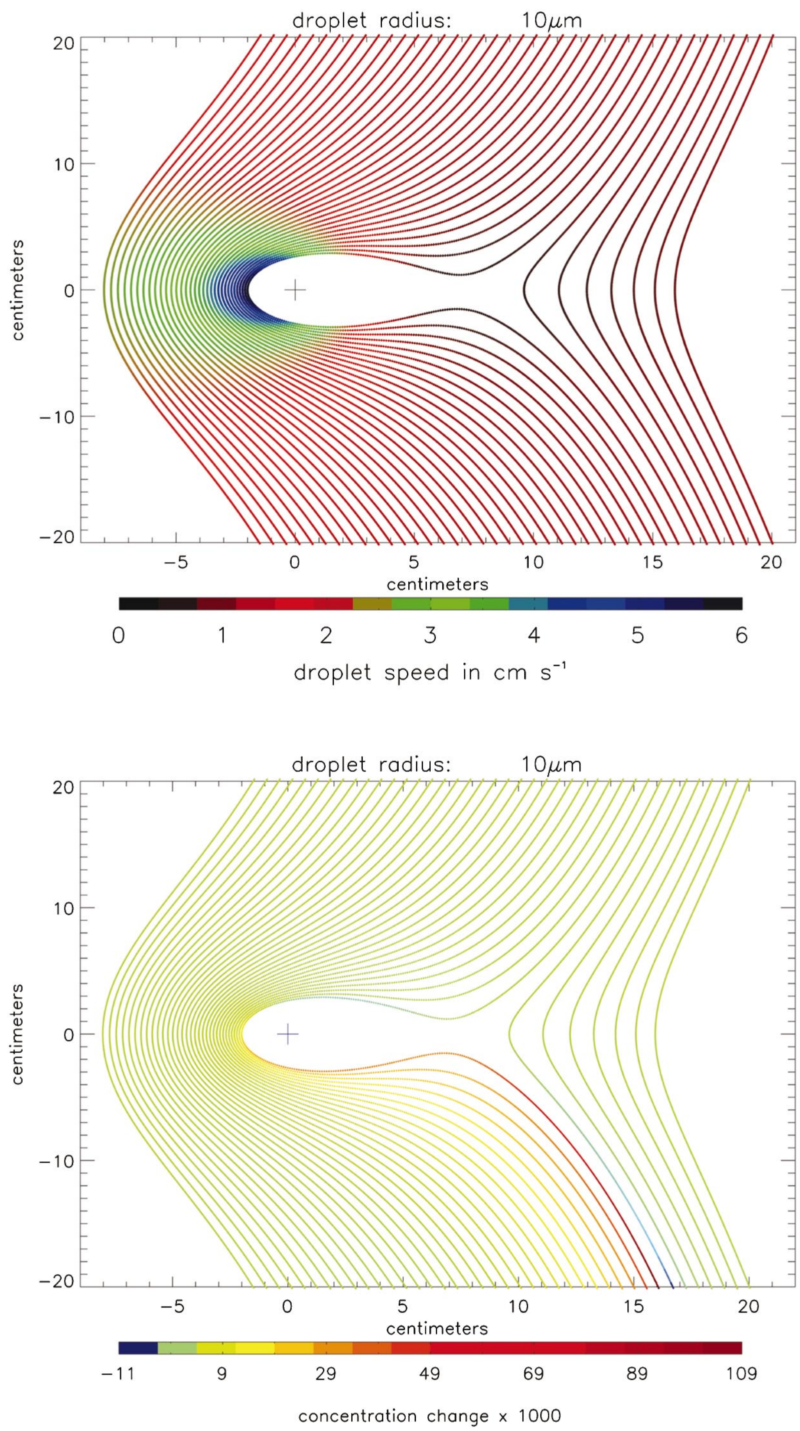

FIG. 1. (Color). Trajectories of droplets of 10 μm radius are shown for the gentle vortex case. Top graph: Speed is in color. Bottom graph: Concentration change defined in (27) is in color. Vortex center is marked by $+$.

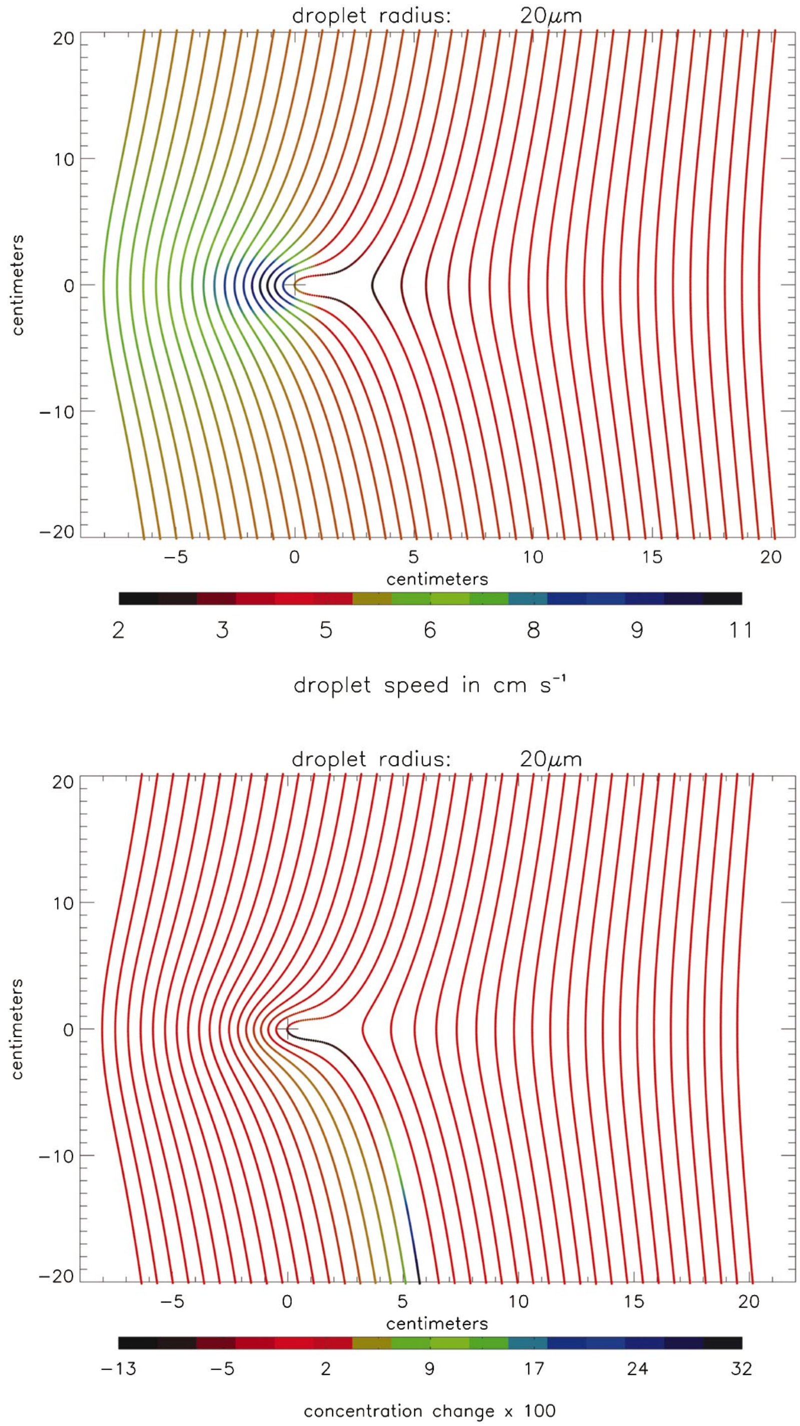

FIG. 2. (Color). Trajectories of droplets of 20 μm radius are shown for the gentle vortex case. Top graph: Speed is in color. Bottom graph: Concentration change defined in (27) is in color. Vortex center is marked by +.

drag, the color indicates the drift speed U_d given in Table II. The slowing of droplets to the right of the center is caused by the updraft there, and the increased speed to the left of the center is caused by the downdraft. For the 10 μm radius droplets, the bottom graph in Fig. 1 shows the same trajectories as in the top graph, but the color quantifies the concentration change defined by

$$[N(\mathbf{x},t)/N_0 - 1]. \tag{27}$$

There is zero concentration change at the top of the graph. A cross marks the vortex center. Below the vortex center there is a concentration enhancement on the trajectories that pass left of the vortex center and a depletion for those that continue downward to the right of vortex center.

Figures 2 and 3 are the same type as Fig. 1, but for 20 μm and 40 μm radius droplets, respectively. Again, the colors at the top of the top graph indicate the drift speeds U_d given in Table II, and there is zero concentration change at the top of the bottom graph. There are no equilibrium points

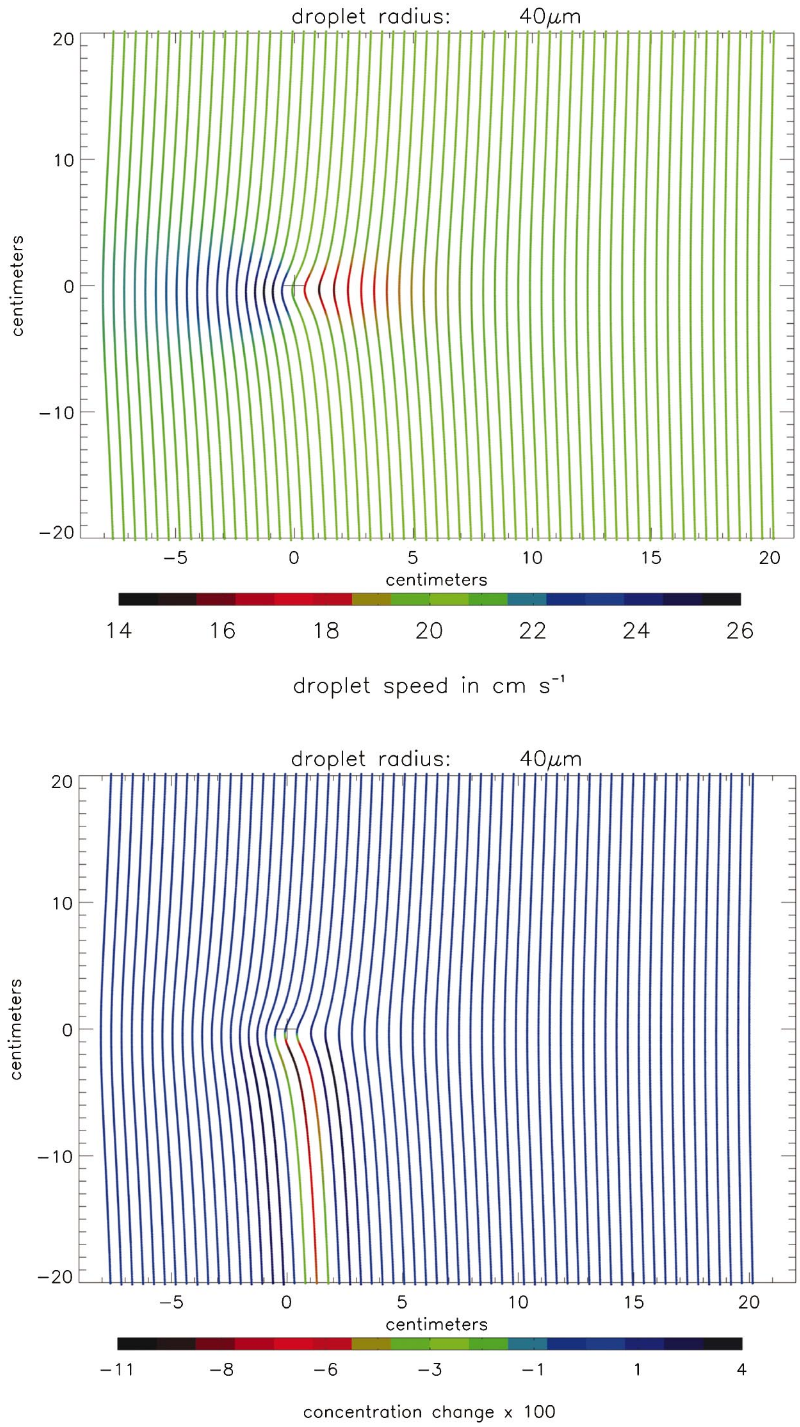

FIG. 3. (Color). Trajectories of droplets of 40 μm radius are shown for the gentle vortex case. Top graph: Speed is in color. Bottom graph: Concentration change defined in (27) is in color. Vortex center is marked by +.

for the 40 μm radius droplets, so the droplets can fall through any point in Fig. 3 (unlike in Figs. 1 and 2). In Fig. 3 there is a concentration depletion (at most 11%) below the center of the vortex with an enhancement (to almost 4%) at both rightward and leftward of the depletion.

The axes in Figs. 1–3 are in centimeters and $r_0=1$ cm such that the axes can be considered dimensionless, i.e., x/r_0, y/r_0 (the vertical axis is compressed by about a factor of 2 relative to the horizontal axis). Because the same spatial domain is shown in Figs. 1–3, it is evident that as the droplet size increases, there is a decrease in the size of the region in which the vortex has a strong influence.

At the rightmost equilibrium point (see Table III), trajectories split into those that go rightward and those that go leftward. Falling from above, 10 μm and 20 μm radius droplets are excluded from an oblong region in Figs. 1 and 2; that region is leftward of the rightmost equilibrium point listed in Table III. Droplets exist in that region only if they are there initially (although, in unsteady flow, droplets could enter a region that is later excluded because of vortex intensification); those trajectories are not part of this study. Fung[56] shows particle trajectories for inertial particles in the excluded region and their residence times therein. Below and to the right of the rightmost equilibrium point, the excluded

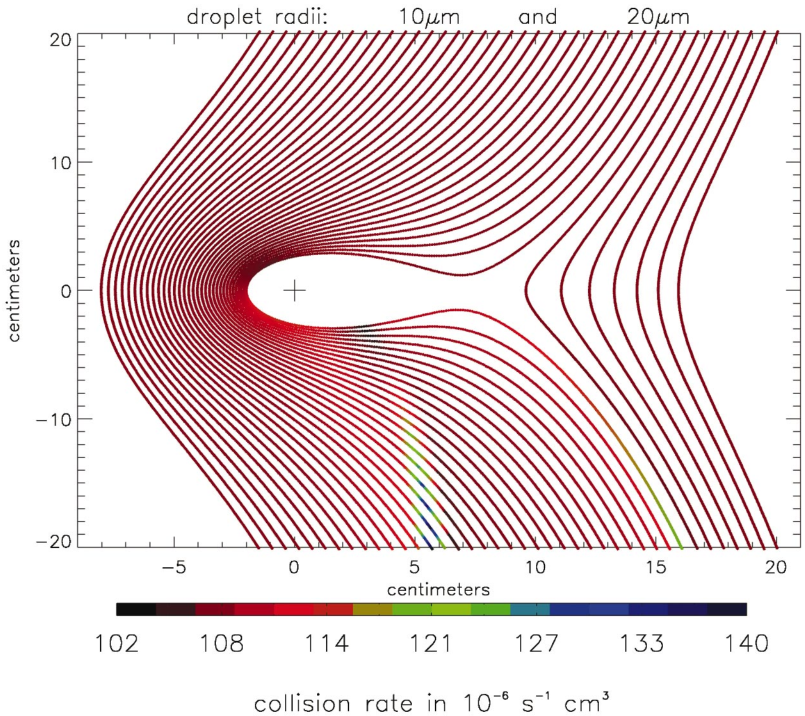

FIG. 4. (Color). For the gentle vortex case, collision rates of droplets of radii 10 and 20 μm are shown in color on the trajectories of the 10 μm droplets. Vortex center is marked by +.

region extends into a narrow gap between the trajectories that sweep around the vortex and those that fall rightward. This gap, in which there are no trajectories, is discussed in detail by Davila and Hunt[52] and is therefore not emphasized here. The gap becomes evident when many trajectories are calculated that pass close to the rightmost equilibrium point.[52] An aspect of the gap is the pileup of trajectories on the leftward side of the gap which results in the concentration increase there that is evident in Figs. 1 and 2; a lesser concentration decrease is seen on the rightward side of the gap.

B. Geometric collision rates

Now that we have concentrations and relative velocities, we can calculate geometric collision rates from (14); for dis-

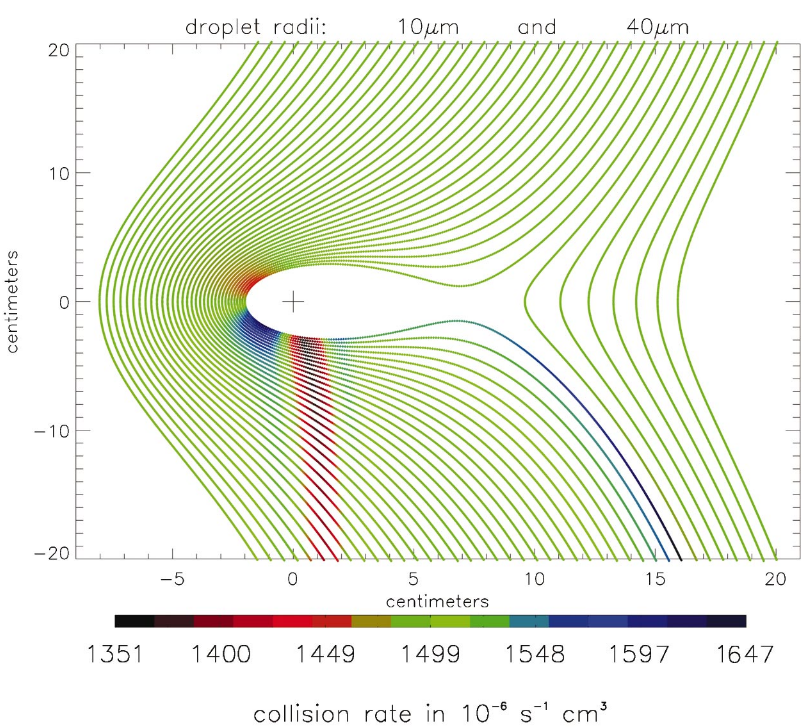

FIG. 5. (Color). For the gentle vortex case, collision rates of droplets of radii 10 and 40 μm are shown in color on the trajectories of the 10 μm droplets. Vortex center is marked by +.

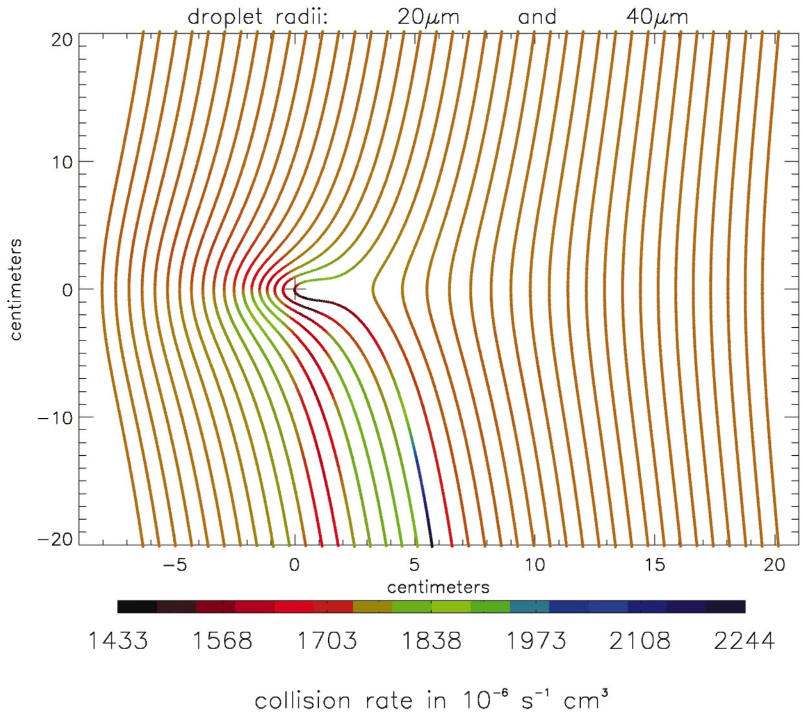

FIG. 6. (Color). For the gentle vortex case, collision rates of droplets of radii 20 and 40 μm are shown in color on the trajectories of the 20 μm droplets. Vortex center is marked by +.

parate particle sizes the contribution of (21) is negligible. For the gentle vortex case, the collision rates are shown in color in Figs. 4–6 for binary collisions of droplets of radius 10 μm with those of 20 μm, 10 μm with 40 μm, and 20 μm with 40 μm, respectively. The collision rate can be calculated only where both sizes of droplets have a trajectory. Since the smaller droplet has trajectories in a lesser volume than the heavier droplet, the collision rates are shown in Figs. 4–6 superimposed on the trajectories of the smaller of the two droplets. Concentrations and velocities of the larger droplet are interpolated to the smaller's trajectories. The collision rate has units of $10^{-6}\ \mathrm{s}^{-1}\ \mathrm{cm}^3$ because it is normalized by both initial concentrations. When interpreting the collision rates, keep in mind that in a cloud that will soon produce rain, droplets of radius 10 μm are about 100 times more numerous than 20 μm droplets, and 20 μm droplets are perhaps 1000 times more numerous than 40 μm droplets. At the top of Figs. 4–6 the collision rate is dominated by the classic mechanism of the larger droplet overtaking the smaller because of the difference in their drift velocities U_d. Nearer to the vortex center, below it, and near the gap, one can see the effect of the concentration change of both droplets as well as that of their relative velocity. In Fig. 2, the lower end of the 20 μm droplet's trajectory that passed almost through the vortex center shows increased concentrations, as do trajectories at near left of that trajectory; these increases are reflected in the increased collision rates at the corresponding positions in Fig. 4, and similarly in Fig. 6. The depletion in concentration below the vortex center for the 40 μm droplets in Fig. 3 is reflected in the decrease of the collision rates at the corresponding spatial positions in Figs. 5 and 6. Below the vortex center in Fig. 1, there is increased concentration of the 10 μm droplets leftward of the gap and decreased concentration rightward of the gap. This is reflected in the collision rates in Figs. 4 and 5. Clearly, spatial variation of relative velocity also modulates the collision rates in Figs. 4–6.

VIII. STRONG VORTEX

A. Droplet trajectories and concentrations

To better show details near the vortex center for the case of the strong vortex, the vertical axes in the figures for the strong vortex case are limited to the range 7–−7 cm, whereas the figures for the gentle vortex case above show the full computation range of 20–−20 cm. Also to better show details, the horizontal range is reduced for the 10 μm droplets relative to the gentle vortex figures, and it is yet further reduced for the 20 and 40 μm droplets. A cross marks the vortex center. As in the gentle vortex figures, the axes are in centimeters, but now $r_0 = 1/3$ cm such that the axes can be considered dimensionless in the form $x/(3r_0)$, $y/(3r_0)$.

For the case of the strong vortex, the top graph in Fig. 7 shows trajectories of droplets of radii 10 μm with color indicating droplet speed, and the bottom graph in Fig. 7 shows concentration change as defined in (27). Figure 7 looks surprisingly similar to Fig. 1. The reason is that ω_0 is ten times larger for Fig. 7 relative to Fig. 1, but r_0 is three times smaller. The rightmost equilibrium point from Table III is at horizontal position $6.9r_0 = 6.9$ cm in Fig. 1 and at $23r_0 = 7.7$ cm in Fig. 7; the fact that the equilibrium points are of similar value causes the similar appearance of those figures. In units of vortex radius r_0, the trajectories are roughly 3.3 times further from the vortex center in Fig. 7 as compared to Fig. 1.

For the 20 μm droplets, the trajectories and velocities are shown in the top graph in Fig. 8, and concentration change is in the bottom graph in Fig. 8. Note that the horizontal range in the top graph is −5–7 cm but only −2–4.6

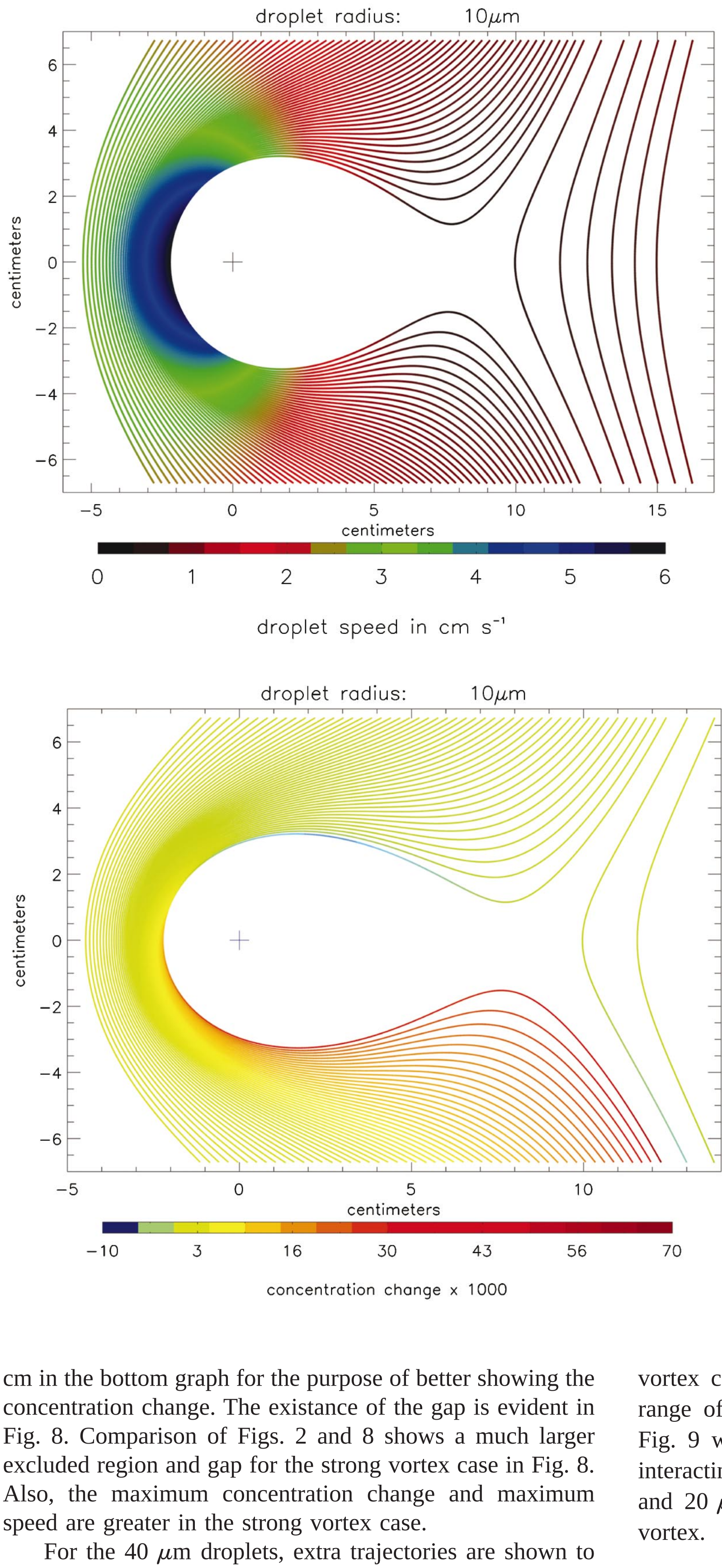

FIG. 7. (Color). Trajectories of droplets of 10 μm radius are shown for the strong vortex case. Top graph: Speed is in color. Bottom graph: Concentration change defined in (27) is in color. The extent of the horizontal axis is reduced relative to the top graph to better show the concentration change. Vortex center is marked by +.

cm in the bottom graph for the purpose of better showing the concentration change. The existance of the gap is evident in Fig. 8. Comparison of Figs. 2 and 8 shows a much larger excluded region and gap for the strong vortex case in Fig. 8. Also, the maximum concentration change and maximum speed are greater in the strong vortex case.

For the 40 μm droplets, extra trajectories are shown to better display details in Fig. 9 because the narrower range of the horizontal axis (−2–2.5 cm) makes the trajectories appear further apart. Although there is no excluded region or gap in Fig. 9, there is one crossing of trajectories. The range of speeds in Fig. 9 is significantly greater than for the gentle vortex case in Fig. 3; a similar observation regarding the range of concentration changes is obtained by comparing Fig. 9 with Fig. 3. This results from the 40 μm droplets interacting with the middle of the vortex. In contrast, the 10 and 20 μm droplets are excluded from the middle of the vortex.

B. Geometric collision rates

The collision rates are given in Figs. 10–12 for binary collisions of droplets of radius 10 μm with those of 20 μm, 10 μm with 40 μm, and 20 μm with 40 μm, respectively.

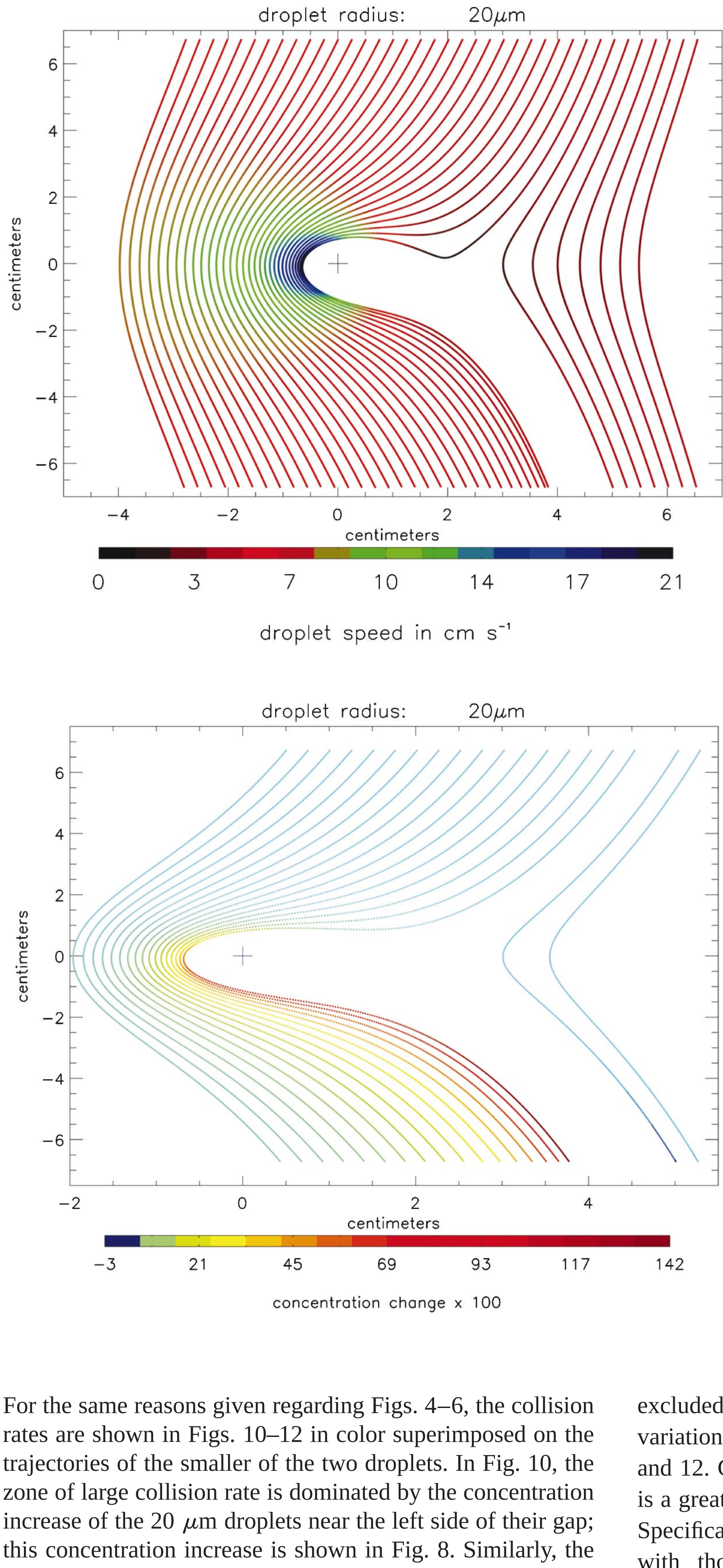

FIG. 8. (Color). Trajectories of droplets of 20 μm radius are shown for the strong vortex case. Top graph: Speed is in color. Bottom graph: Concentration change defined in (27) is in color. The extent of the horizontal axis is reduced relative to the top graph to better show the concentration change. Vortex center is marked by +.

For the same reasons given regarding Figs. 4–6, the collision rates are shown in Figs. 10–12 in color superimposed on the trajectories of the smaller of the two droplets. In Fig. 10, the zone of large collision rate is dominated by the concentration increase of the 20 μm droplets near the left side of their gap; this concentration increase is shown in Fig. 8. Similarly, the variation of the concentration of the 40 μm droplets in Fig. 9 in the region that is below and to the right of the vortex center is seen to dominantly modulate the values of collision rates in Figs. 11 and 12. The large variation of droplet velocity of the 40 μm droplets seen in Fig. 9 occurs mostly in the excluded region of the smaller droplets; hence, those velocity variations have little effect on the collision rates in Figs. 11 and 12. Comparing the gentle and strong vortex cases, there is a greater range of collision rates in the strong vortex case. Specifically, for the collision of droplets of radius 10 μm with those of 20 μm, the range of collision rates is $(1 \text{ to } 1.4)\times 10^{-4}\ \mathrm{s}^{-1}\ \mathrm{cm}^3$ for the gentle vortex case in Fig. 4 as compared to $(1 \text{ to } 5)\times 10^{-4}\ \mathrm{s}^{-1}\ \mathrm{cm}^3$ in the strong vortex case of Fig. 10. Similarly, for collisions of 10 μm with 40 μm droplets, the range of collision rates is (13 to 16)

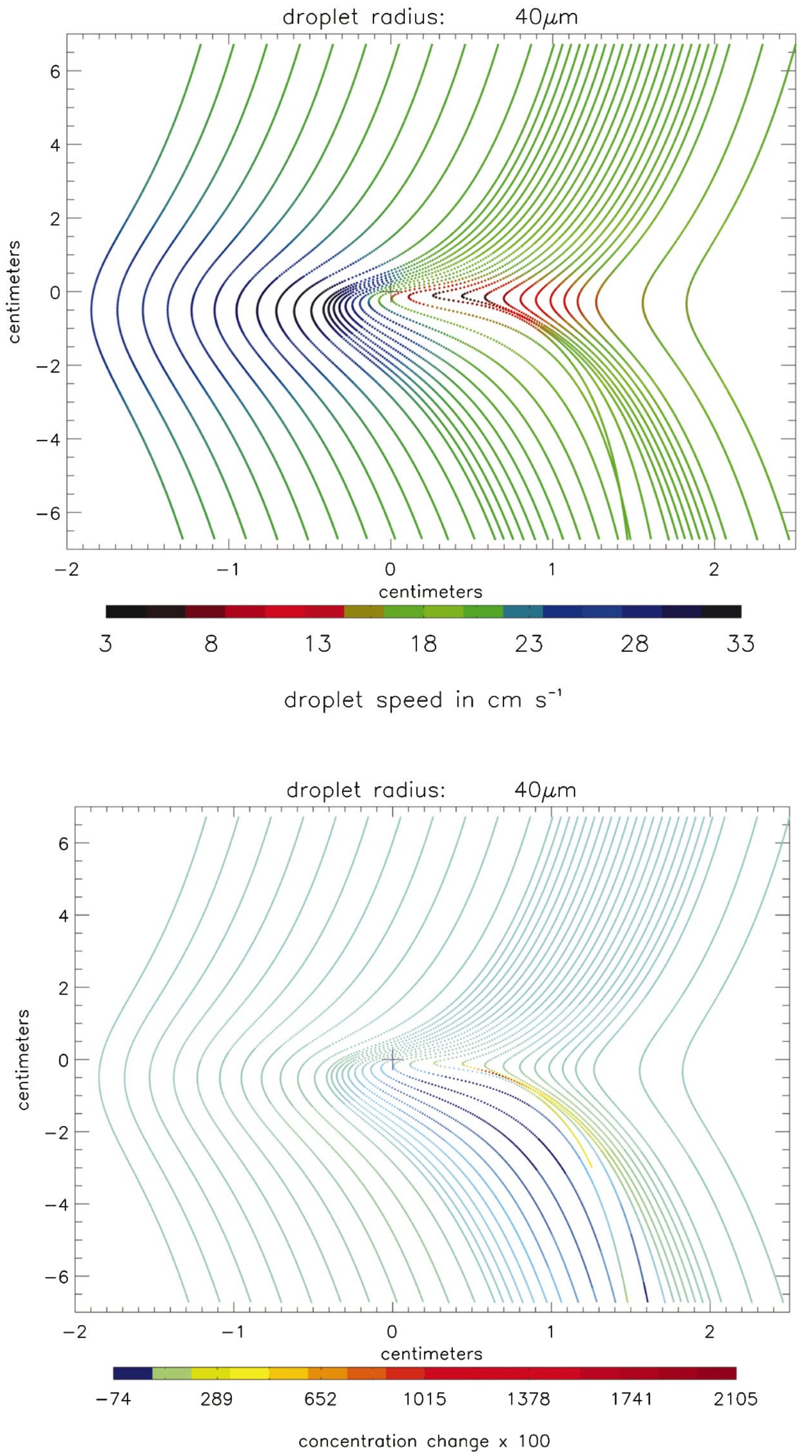

FIG. 9. (Color). Trajectories of droplets of 40 μm radius are shown for the strong vortex case. Top graph: Speed is in color. Bottom graph: Concentration change defined in (27) is in color. Vortex center is marked by $+$.

$\times 10^{-4}\ \mathrm{s}^{-1}\,\mathrm{cm}^3$ versus $(3\ \text{to}\ 30)\times 10^{-4}\ \mathrm{s}^{-1}\,\mathrm{cm}^3$, and is $(14\ \text{to}\ 22)\times 10^{-4}\ \mathrm{s}^{-1}\,\mathrm{cm}^3$ versus $(6\ \text{to}\ 120)\times 10^{-4}\ \mathrm{s}^{-1}\,\mathrm{cm}^3$ for collisions of 20 μm with 40 μm droplets. The figures show the spatial variation of collision rates, but the results do not lend themselves to determination of a single number such as the space-averaged collision rate. This is because space-averaged rate depends on the volume of the average; it must approach the gravitationally induced collision rate as the volume increases.

IX. APPROXIMATE EQUATIONS OF MOTION

The limits of applicability of approximations to the equations that we have solved are discussed next. By graphing the terms in the differential equations, we determine under what conditions some of these terms may be neglected. Neglect of these terms can simplify the equations but may or may not simplify the computation. The spin deflection term in (9), i.e., $D\mathbf{S}\times(\mathbf{w}+\hat{\mathbf{g}})$, is orders of magnitude smaller than the other terms. This term is always negligible in the present

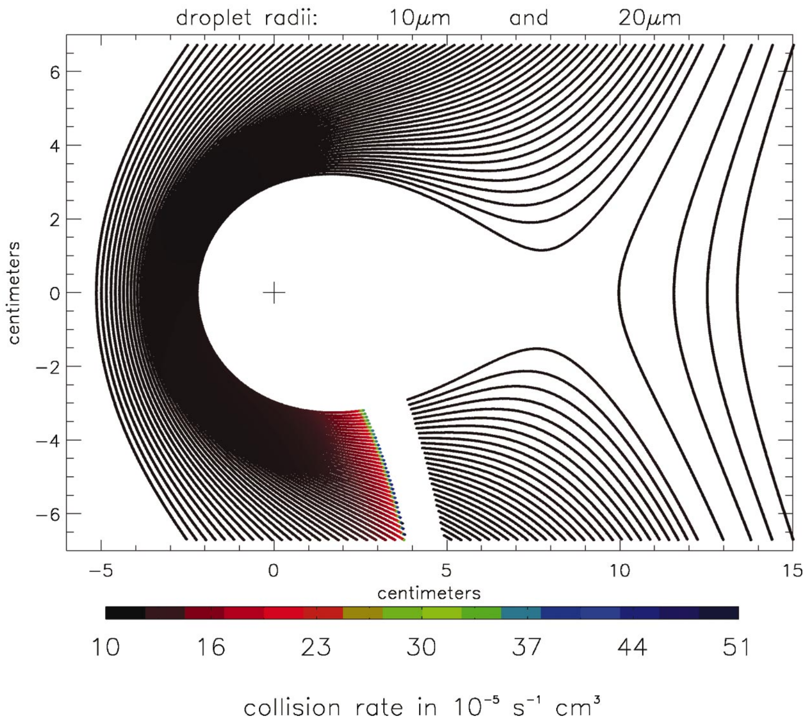

FIG. 10. (Color). For the strong vortex case, collision rates of droplets of radii 10 and 20 μm are shown in color on the trajectories of the 10 μm droplets. Vortex center is marked by $+$.

calculations (perhaps not so in all possible calculations). Neglect of the spin deflection is a significant simplification to the computation because (10) and (A3) need not be solved, and the air-flow quantities within these equations need not be evaluated, but there is negligible savings of computation time.

A. Approximate equations of motion: Gentle vortex

The equations of droplet motion (9) are solved in two-dimensional (2D) Cartesian coordinates: horizontal denoted by unit vector $\hat{\mathbf{x}}$ or subscript x, e.g., $V_x = \hat{\mathbf{x}} \cdot \mathbf{V}$, and vertical denoted by unit vector $\hat{\mathbf{y}}$ or subscript y. Note that $\hat{\mathbf{y}}$ is oppo-

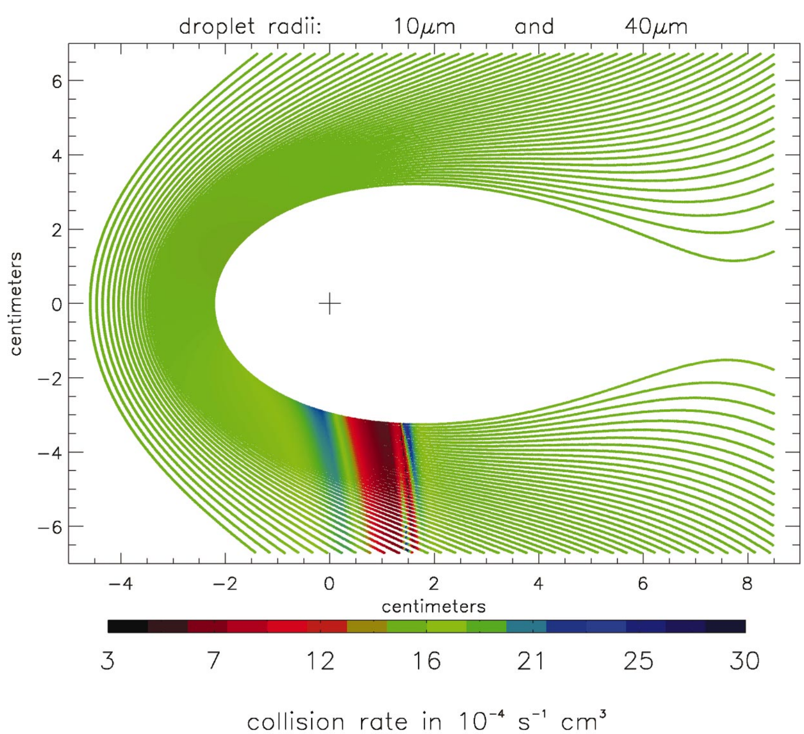

FIG. 11. (Color). For the strong vortex case, collision rates of droplets of radii 10 and 40 μm are shown in color on the trajectories of the 10 μm droplets. Vortex center is marked by $+$.

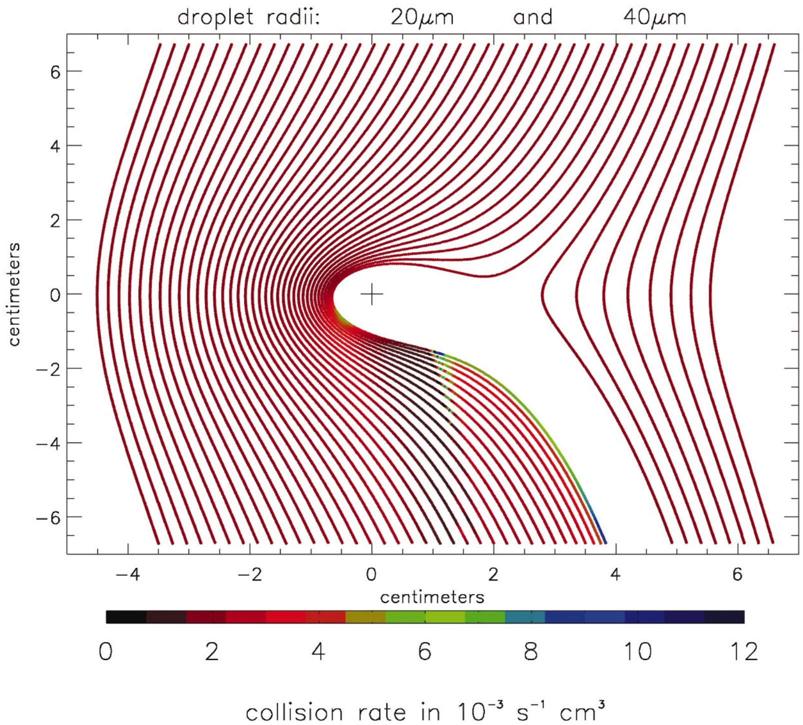

FIG. 12. (Color). For the strong vortex case, collision rates of droplets of radii 20 and 40 μm are shown in color on the trajectories of the 20 μm droplets. Vortex center is marked by +.

site to the direction of gravity; $\hat{\mathbf{y}}=-\hat{\mathbf{g}}$. The horizontal component of terms in the differential equation (9) are shown for the gentle vortex in Fig. 13; top, middle, and bottom graphs in Fig. 13 are for droplet radii 10 μm, 20 μm, and 40 μm, respectively. The terms in the differential equation are shown for the trajectory that passes closest to the vortex center. The abscissa is the time in units of the droplet relaxation time τ_d since the beginning of the trajectory. For the 10 μm radius, only the middle of the trajectory is graphed to avoid compressing that portion into a small fraction of the graph. The vertical components of terms in (9) are qualitatively similar to the horizontal components; they differ in details, of course. Similar conclusions are obtained when other trajectories are studied, including the trajectories that remain rightward of the rightmost equilibrium point. Because the terms vary by orders of magnitude along the trajectory, their absolute value is graphed on a logarithmic scale; those times when a term changes sign are seen as abrupt minima in its curve.

For the 40 μm droplets, the two terms $-BD\mathbf{u}/Dt$ and $-(\mathbf{w}+\hat{\mathbf{g}})\cdot\nabla\mathbf{u}$ closely cancel each other except near the center of the trajectory; therefore, an extra curve equal to their sum, $|\hat{\mathbf{x}}\cdot(-BD\mathbf{u}/Dt-(\mathbf{w}+\hat{\mathbf{g}})\cdot\nabla\mathbf{u})|$, is shown in Fig. 13. For this case, the significance of the history integral, as well as the other terms, can be judged relative to $-BD\mathbf{u}/Dt-(\mathbf{w}+\hat{\mathbf{g}})\cdot\nabla\mathbf{u}$ rather than to $-BD\mathbf{u}/Dt$ and $-(\mathbf{w}+\hat{\mathbf{g}})\cdot\nabla\mathbf{u}$ separately. One sees in Fig. 13 that the history integral is an important term for the 40 μm droplets except when the droplet is close to the vortex center. The history integral is seen to be significant all along the trajectories of the 10 and 20 μm droplets. The hysteresis effect of the history integral is seen to cause an asymmetry to the curves plotted versus time in Fig. 13.

The term $d\mathbf{w}/dt$ becomes rapidly negligible as droplet radius decreases; this is true for all trajectories of 10 and 20 μm droplets (for this gentle vortex flow, of course); that fact is shown for $|dw_x/dt|$ in Fig. 13 and is also true for the vertical component $|dw_y/dt|$. This means that, for a small enough radius, $d\mathbf{w}/dt$ can be neglected within the history integral as well as on the left-hand side of (9); this is true for the gentle vortex case for 10 and 20 μm droplets, but not 40 μm droplets. Then, neglecting $d\mathbf{w}/dt$, a simplified equation of motion can be solved, namely [after multiplication of (9) by -1],

$$0 \simeq A\mathbf{w} + B\frac{D\mathbf{u}}{Dt} + (\mathbf{w}+\hat{\mathbf{g}})\cdot\nabla\mathbf{u} + C\int_{-\infty}^{t} dt' \times[(\mathbf{w}+\hat{\mathbf{g}})\cdot\nabla\mathbf{u}](t-t')^{-1/2}. \tag{28}$$

The scaled version of (7) is $d\mathbf{w}/dt=d\mathbf{V}/dt-D\mathbf{u}/Dt-(\mathbf{w}+\hat{\mathbf{g}})\cdot\nabla\mathbf{u}$; since Fig. 13 and similar results for the vertical component show that $d\mathbf{w}/dt$ may be neglected relative to $BD\mathbf{u}/Dt$ and $(\mathbf{w}+\hat{\mathbf{g}})\cdot\nabla\mathbf{u}$ or their sum, we have

$$\frac{d\mathbf{V}}{dt} \simeq \frac{D\mathbf{u}}{Dt} + (\mathbf{w}+\hat{\mathbf{g}})\cdot\nabla\mathbf{u} \tag{29}$$

for the 10 and 20 μm droplets. This is not true in Fig. 13 for the 40 μm droplets. Then, for the above limited cases, substitution of (29) in (28) shows that (28) can also be written as

$$\frac{d\mathbf{V}}{dt} \simeq -\mathbf{w} - C\int_{-\infty}^{t} dt'(\mathbf{w}+\hat{\mathbf{g}})\cdot\nabla\mathbf{u}\left[(t-t')^{-1/2}\right], \tag{30}$$

where $A\simeq 1$ and $B\simeq 1$ were used. For purposes of reducing the difficulty of solving the equations, (30) is not simpler than (28). The history integral is not negligible in (30) for either the horizontal or vertical components; thus (30) gives $d\mathbf{V}/dt \neq -\mathbf{w}$, which, when unscaled, is

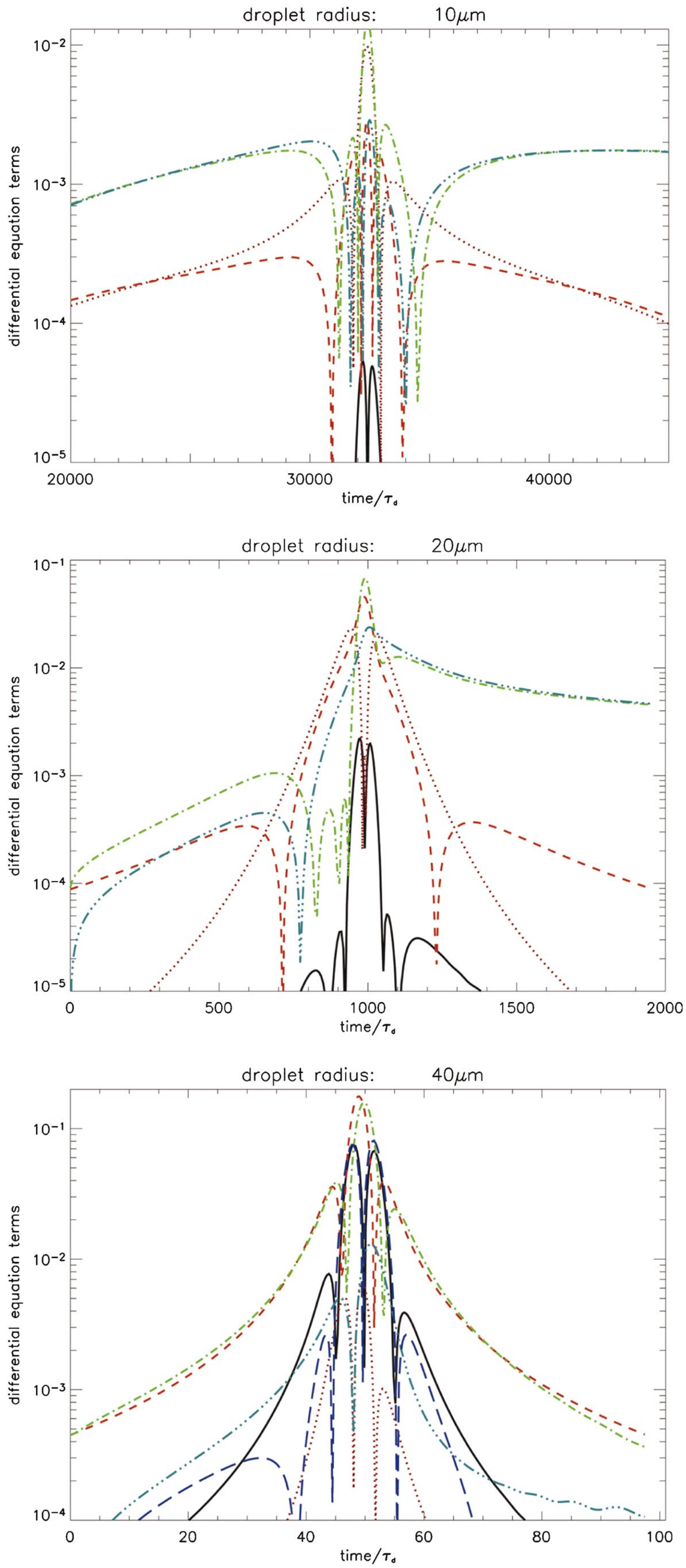

FIG. 13. (Color). For the gentle vortex case, the absolute magnitudes of the horizontal component of terms in (9) are shown vs t/τ_d for the trajectory that passes closest to the vortex center. Solid black: $|dw_x/dt|$. Dotted red: $|-Aw_x|$. Short-dashed orange: $|-BDu_x/Dt|$. Dash-dot green: $|-(\mathbf{w}+\hat{\mathbf{g}})\cdot\nabla u_x|$. Dash-dot-dot-dot light blue: history integral. Long-dashed dark blue: $|-BDu_x/Dt-(\mathbf{w}+\hat{\mathbf{g}})\cdot\nabla u_x|$. Text states which trajectory was used.

$$m_d \frac{d\mathbf{V}}{dt} \neq (m_d - m_f)\mathbf{g} - 6\pi a \mu (\mathbf{V} - \mathbf{u}) \quad \text{(unscaled)}. \tag{31}$$

It is significant that (31) with $\neq$ replaced by $=$ does appear ubiquitously in the literature (e.g., as described by Kim *et al.*[39]). Use of (29) and Fig. 13 shows that the history integral should not be neglected relative to $m_d d\mathbf{V}/dt$. Note that the above approximations are not true for the 40 μm droplets because Fig. 13 shows that only the spin deflection term in (9) can be neglected for the horizontal component, and the same is true for the vertical component.

The magnitudes of terms in Fig. 13 have more than just relative meaning. Return to the scaled variable notation (i.e., $\tilde{}$) and note that the maximum values of $|\widetilde{-Aw_x}|$ in Fig. 13 increase for the horizontal-component equation from about 0.006 to 0.02 as droplet radii decrease from 40 μm to 10 μm. Not shown is the corresponding decrease of $|\widetilde{-Aw_y}|$ as droplet radius decreases by about 0.03 to 0.006. All the other trajectories (that are not shown in the figures) have yet smaller maxima in $|\widetilde{-Aw_x}|$ and $|\widetilde{-Aw_y}|$. The fact that $|\widetilde{-Aw_y}| \lesssim 0.03$ is equivalent to the fact that the sum of all terms other than $-\widetilde{Aw_y}$ in the vertical component of (9) equals $-\widetilde{Aw_y}$ such that $|\widetilde{-Aw_y}|$ is small compared to unity. The scaled version of (6) is $-\tilde{\mathbf{w}} = \hat{\mathbf{g}} - (\tilde{\mathbf{V}} - \tilde{\mathbf{u}})$; because $A \simeq 1$, it follows that

$$-\widetilde{Aw_y} \simeq -1 - (V_y - u_y)/U_d.$$

Because the left-hand side has magnitude 0.03 or less and the right-hand side contains unity, the two terms on the right-hand side cancel to about 3% or less. That is, to an error of 3% or less

$$0 \simeq U_d + (V_y - u_y) \quad \text{(unscaled)}. \tag{32}$$

There is no corresponding approximation for the horizontal component V_x other than $|V_x - u_x| \lesssim 0.03U_d$. Of course, (32) is the approximation that V_y is the drift speed U_d relative to the vertical component of the local flow u_y. The facts that the slip-velocity's vertical component $V_y - u_y$ differs little from $-U_d$ and that $|V_x - u_x| \lesssim 0.03U_d$ supports use of U_d in our definition of droplet Reynolds number, i.e., $R_d \equiv U_d a/\nu$.

As radius is reduced, computation time for (9) increases greatly for two reasons. First, the droplets fall more slowly such that the time for them to fall out of the computation volume increases, as evidenced by the larger values on the abscissa of the top graph in Fig. 13 as compared to the bottom graph. Second, a greater number of time steps per τ_d is required for accuracy, and the integrand of the history integrand must be stored for each time step. Consequently, use of (32) becomes useful and becomes more accurate as droplet radius is reduced much below 10 μm. Approximations have not been used in this study.

The above agrees in detail with Manton's[57] scaling of the equation of motion and its approximation, except that his neglect of the history integral is contradicted.

B. Approximate equations of motion: Strong vortex

The horizontal component of terms in the differential equation (9) are shown for the strong vortex in Fig. 14 for droplet radii 10 μm, 20 μm, and 40 μm, respectively. The trajectories used for Fig. 14 are second to the last trajectory that passes leftward of the vortex center in Fig. 7 (for the 10 μm droplets) and in Fig. 8 (for the 20 μm droplets). The trajectory used for the 40 μm droplets in Fig. 14 is the twelfth from the left of the closely spaced trajectories in Fig. 9; it is the third trajectory that turns at the right side of the vortex center. Similar conclusions are obtained when other trajectories are studied. Similar to the gentle vortex case in Fig. 13, the absolute values of the terms are graphed on a logarithmic scale; as before, the vertical components of terms in (9) are qualitatively similar to the horizontal components. Only the middle of the trajectories are graphed in Fig. 14 to avoid compressing that portion into a small fraction of the graph. As in the gentle vortex case, the spin deflection term in (9), i.e., $D\mathbf{S} \times (\mathbf{w} + \hat{\mathbf{g}})$, is orders of magnitude smaller than the other terms and is therefore far below the bottom axes on Fig. 14; that term is always negligible. For the 40 μm radius, an extra curve equal to $|\hat{\mathbf{x}} \cdot (-BD\mathbf{u}/Dt - (\mathbf{w} + \hat{\mathbf{g}}) \cdot \nabla \mathbf{u})|$ is shown (the long-dashed curve), but unlike the gentle vortex case, the two terms $-BD\mathbf{u}/Dt$ and $-(\mathbf{w} + \hat{\mathbf{g}}) \cdot \nabla \mathbf{u}$ closely cancel each other only on the upper part of the trajectory.

For the 10 μm radius, the entire horizontal extent of the top graph in Fig. 14 is remarkably similar to the middle one-third of the gentle vortex case in Fig. 13. (More of the trajectory is shown in the latter figure.) This similarity corresponds to the similarity in the top graphs of Figs. 7 and 1, which was explained in Sec. VIII A; briefly, the 10 μm droplets are excluded from such a large central region of the strong vortex that the flow they encounter is relatively quiescent. One concludes that the approximations to the differential equations deduced above for the 10 μm droplets in the gentle vortex case also apply to the 10 μm droplets in the strong vortex case. Specifically, (28), (30), and (32) apply.

For the 20 μm droplets, comparison of Fig. 14 for the strong vortex case with the gentle vortex case in Fig. 13 shows that the time-derivative term $d\mathbf{w}/dt$ is not negligible in the strong vortex case because $|dw_x/dt|$ rises to within about 1/5 or the largest term in Fig. 14 as compared to about 1/30 of the largest term in Fig. 13; although not shown, the same is true for the other component $|dw_y/dt|$. Also, the term $|-Aw_x|$ is larger in the strong vortex case. In the $a = 20$ μm graph in the middle of Fig. 14, the maximum of $|-Aw_x|$ is 0.32 where $V_x - u_x = 0.32U_d$. One maximum of $|-Aw_y|$ (not shown) is where $V_y - u_y = -0.47U_d$ and another is where $V_y - u_y = -1.24U_d$; in contrast, (32) gives $V_y - u_y = -U_d$. Following the discussion in Sec. IX A, one sees that none of the approximations (28), (30), and (32) applies to the strong vortex case for 20 μm droplets. That is, except for the neglect of the spin deflection term $D\mathbf{S} \times (\mathbf{w} + \hat{\mathbf{g}})$, Eq. (9) must be solved.

For the 40 μm droplets, the above conclusions regarding the 20 μm droplets are even more strongly confirmed. Specifically, in the $a = 40$ μm graph at the bottom of Fig. 14, the time-derivative term $|dw_x/dt|$ has the largest maximum value of all terms, namely, 0.6. The vertical component $|dw_y/dt|$ also has the largest maximum value, namely, 0.6. The maxi-

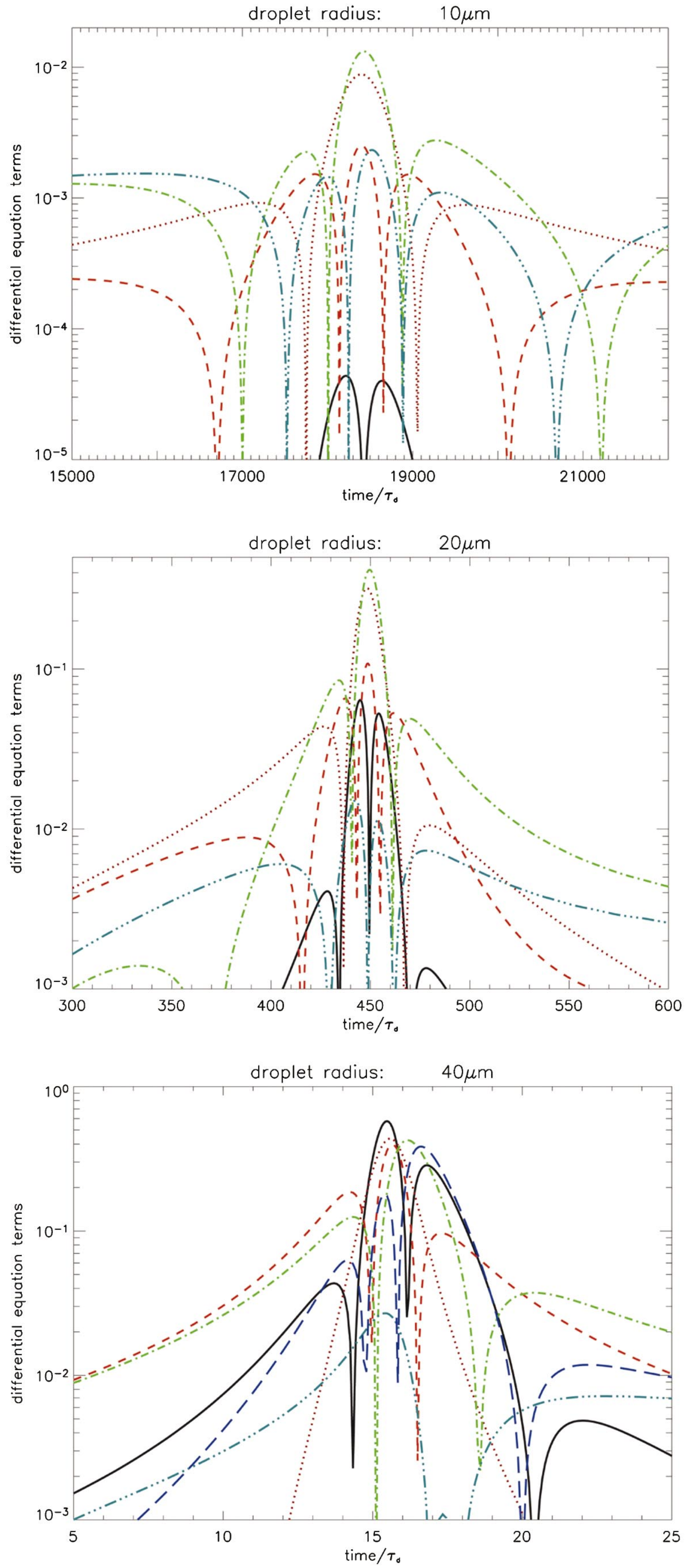

FIG. 14. (Color). Same as Fig. 13 except for the strong vortex case.

mum of $|-Aw_x|$ is 0.44, where $V_x - u_x = 0.44U_d$. The maximum of $|-Aw_y|$ is where $V_y - u_y = -0.47U_d$, whereas (32) gives $V_y - u_y = -U_d$.

C. Approximations for the other equations

Equations (10) for $\mathbf{S}$, (A2) for $\partial \mathbf{w}/\partial x_0$, and (A3) for $\partial \mathbf{S}/\partial x_0$ can be studied by the same method as used above. For (A2) and (A3) one finds that their important terms are those that correspond to the terms that dominate in the equations from which they were derived, namely, (9) and (10), respectively.

Now consider (10). Recall that $D\omega/Dt = 0$ in our flow. For spin $\mathbf{S}$ the three nonzero terms in (10) are of the same order of magnitude for droplets of 40 μm radius ($d\mathbf{S}/dt$ is the smallest of the terms at most points), but $d\mathbf{S}/dt$ quickly becomes smaller with decreasing radius, and it is negligible for 10 μm radius. The 20 μm droplets pass through and close to the vortex center where vorticity is large in the gentle vortex case; nevertheless, $d\mathbf{S}/dt$ is not more than about 2% of the other terms. Thus, for the smaller droplets (10) becomes the algebraic equation $\mathbf{S} = (3/20)(\mathbf{w} + \hat{\mathbf{g}}) \cdot \boldsymbol{\nabla}\omega$. Reverting to the tilde notation ($\tilde{\ }$) for scaled variables and using $|\tilde{\mathbf{w}} + \hat{\mathbf{g}}| \simeq 1$, $|\tilde{\mathbf{S}}| \simeq 0.15|\cos(\varphi) d\tilde{\omega}/d\tilde{r}|$, where φ is the angle between $\tilde{\mathbf{w}} + \hat{\mathbf{g}}$ and the radial direction. For our vorticity (22), we have $|\tilde{\mathbf{S}}| \simeq 0.3\omega(r)\tau_d \ell_d r/r_0^2 |\cos(\varphi)|$; unscaled, this gives $|\mathbf{S}|/[\omega(r)/2] \simeq 0.6\ell_d r/r_0^2|\cos(\varphi)|$. In Fig. 1 for 10 μm radius, for example, on the trajectory closest to the vortex center, we have $r/r_0 \simeq 2.5$ (recall $r_0 = 1$ cm) such that $|\mathbf{S}|/[\omega(r)/2] < 3 \times 10^{-3}$. Similarly, at any point on trajectories of the 20 μm droplets where vorticity is large, e.g., $r/r_0 < 1$ in Fig. 2, we have $|\mathbf{S}|/[\omega(r)/2] < 2 \times 10^{-2}$. Recalling the definition $\mathbf{S} \equiv \boldsymbol{\Omega} - \omega/2$ and that $\omega(r)/2$ is the magnitude of the angular velocity of the flow, one sees that 10 μm and 20 μm droplets are spinning with the flow to excellent approximation. Further, at $r/r_0 \simeq 2.5$, the largest magnitude of the term $-D\tilde{\mathbf{S}} \times (\tilde{\mathbf{w}} + \hat{\mathbf{g}})$ in (9) for 10 μm radius is about $D|\tilde{\mathbf{S}}| \simeq 7 \times 10^{-4}[0.75 \exp(-2.5^2)]\omega_0 \tau_d \ell_d / r_0 \simeq 4 \times 10^{-11}$, which explains why $-D\tilde{\mathbf{S}} \times (\tilde{\mathbf{w}} + \hat{\mathbf{g}})$ is negligible and why its curve does not appear in the figures (for the two larger droplets, use scaling with $\tau_d \ell_d$).

X. DISCUSSION AND CONCLUSION

The equations of motion of water droplets in air were calculated to determine trajectories, velocities, and the change of concentration caused when droplets fall into a vortex. Droplet radii were chosen on the basis of relevance to rain initiation in atmospheric clouds. The resultant geometrical collision rates show the effects of both the relative velocity of droplets as well as their concentrations. Relative to gravitationally induced collision rates, locations of both increased and decreased collisions are shown. The collision rates do not lend themselves to being reduced to a single number for the case presented; for example, a volume average depends on the volume used in the average.

Approximate equations are determined on the basis of the relative values of terms in the differential equations as functions of position on trajectories. It must be kept in mind that the validity of approximations depends on the specific flow and droplet radii studied here. Other flows and radii require further study. For both the gentle and strong Burgers vortex cases studied here, the spin deflection term in (9) is always negligible. For ancillary equations (A2) and (A3), one finds that their important terms are those that correspond to the terms that dominate in the equation from which they are derived.

Approximations applicable to the equation of droplet velocity (9) were studied. First consider the case of the gentle vortex. For the 10 and 20 μm droplets, but not the 40 μm droplets, the angular velocity of the droplets is approximately equal to the angular velocity of the air. The history integral is an important term for all three droplet radii: 10, 20, and 40 μm. The term $d\mathbf{w}/dt$ becomes rapidly negligible as droplet radius decreases. Neglecting $d\mathbf{w}/dt$ gives the approximate equation of droplet motion (28), which can be approximately written as (30); those equations are valid for 10 and 20 μm droplets, but not for 40 μm droplets. In particular, (31) is obtained; that is, the equation of motion most frequently used is inaccurate because the history integral is not negligible. The importance of the history integral, even for small m_f/m_d, is in agreement with calculations by Armenio and Fiorotto.[29] To an accuracy of about 3%, the approximation (32) applies.

Now consider the strong vortex case for approximation to (9). For 10 μm droplets, the same approximate equations are valid in the strong vortex case as in the gentle vortex case, namely, (28), (30), and (32); this fact is related to the extent of the excluded region such that 10 μm droplets do not enter the region of strong vorticity. Unlike the gentle vortex case, those approximations are not valid for 20 μm droplets. None of (28), (30), and (32) is valid for 40 μm droplets in the strong vortex case. The history integral cannot be neglected.

It is preferable to base our understanding of the important terms in the equations of motion on data such as Figs. 13 and 14 as compared to generalized flow parameters like the Froude and Stokes numbers in Tables I and III, which are based on the maximum values of acceleration and velocity gradient. A case in point is that the relative values of $|-BD\mathbf{u}/Dt|$ and $|-(\tilde{\mathbf{w}} + \hat{\mathbf{g}}) \cdot \tilde{\nabla}\tilde{\mathbf{u}}|$ in Fig. 1 are opposite to the expectation based on the Froude and Stokes numbers because, for 10 μm radius the trajectory closest to the vortex center lies significantly beyond the r position of those maxima of acceleration and velocity gradient.

The computations presented here suggest further investigations. The radial inflow of the Burgers vortex could be included. This case would be especially different for the 10 μm droplets in the strong vortex because the smaller droplets will be swept closer to the vortex center by the inward flow, and there would be a smaller excluded region. Calculations could be performed using other droplet sizes and other strengths of vortices. Droplets' motion in other flows could be calculated, for example, strained-spiral vortices and nonstationary flows including DNS of turbulence. The present computer program is applicable to 3D nonstationary flows. One could study droplets within the excluded region. This is a more difficult computation because the vortex must be nonstationary and increasing in maximum vorticity such that droplets are entrained into the volume that will become the excluded region. Of particular interest for that case is the exit of the droplets through the gap as well as the collision rates of equal-sized droplets.

The present calculation is for droplets falling into a Burgers vortex from above; the flow deflects 10 and 20 μm droplets from positions where the accelerations are greatest, despite the fact that those maximum accelerations have probability greater than 10^{-2} (Sec. VI A). Therefore, the greatest flow accelerations experienced by droplets in a cloud are within the excluded region of this study. Vortices of greater maximum acceleration and lesser probability of occurrence might be more significant to the coalescence of droplets, particularly so for droplets within the excluded region. The present study suggests that acceleration-induced coalescence is most significant for droplets that are entrained into or formed within an intensifying vortex as distinct from falling toward the vortex.

Calculation of geometric collision rates in vortices is a step toward understanding droplet coalescence in liquid clouds. Another part of the understanding of coalescence is determining the collision efficiency E, which is the ratio of the number of collisions to the number of geometric collisions. Droplets falling because of gravity in still air have $E<1$ because squeezing flow[58] causes a repulsive force.[58] Rogers and Yau[7] tabulate E for that case: $E<0.053$ for droplets of radius 10 μm colliding with smaller droplets, $E\simeq 0.17$ for 10 μm and 20 μm droplets, $E\simeq 0.55$ for 10 μm with 40 μm, and $E\simeq 0.75$ for 20 μm with 40 μm. Instead of the still-air model, the hydrodynamic interaction of droplet pairs of various radii within local vorticity and strain-rate fields must be determined. For this case, the collision efficiency might be much different as compared to the still-air model. Existing empirical probability density functions of vorticity[17] and acceleration[14] in high Reynolds-number turbulence are also part of the calculation of collision kernels for use in understanding rain initiation from liquid-water clouds.

ACKNOWLEDGMENTS

This work has been supported by the Office of Naval Research Award No. N0001404IP20013 and the NOAA/OGP CLIVAR Program.

APPENDIX

The partial derivative of any flow quantity evaluated at a point on the trajectory $\mathbf{x}(t)$, be it $\mathbf{u}$, $D\mathbf{u}/Dt$, ω, $D\omega/Dt$, etc., is obtained from the spatial derivatives of the flow quantities, e.g., for $\mathbf{u}$:

$$\frac{\partial \mathbf{u}}{\partial x_0} = \left(\frac{\partial \mathbf{x}}{\partial x_0}\cdot\frac{\partial}{\partial \mathbf{x}}\right)\mathbf{u} = \frac{\partial \mathbf{x}}{\partial x_0}\cdot \nabla \mathbf{u}. \tag{A1}$$

Differentiating (11) gives the equation for $\partial\mathbf{x}/\partial x_0$:

$$\frac{d}{dt}\frac{\partial \mathbf{x}}{\partial x_0} = \frac{\partial \mathbf{u}}{\partial x_0} + \frac{\partial \mathbf{w}}{\partial x_0} = \frac{\partial \mathbf{x}}{\partial x_0}\cdot \nabla \mathbf{u} + \frac{\partial \mathbf{w}}{\partial x_0}.$$

Since this equation requires $\partial\mathbf{w}/\partial x_0$, we obtain an equation for $\partial\mathbf{w}/\partial x_0$ by differentiating (9):

$$\begin{aligned}\frac{d}{dt}\frac{\partial \mathbf{w}}{\partial x_0} = & -A\frac{\partial \mathbf{w}}{\partial x_0} - B\frac{\partial}{\partial x_0}\frac{D\mathbf{u}}{Dt} - \frac{\partial \mathbf{w}}{\partial x_0}\cdot\nabla\mathbf{u} - (\mathbf{w}+\hat{\mathbf{g}}) \\ & \cdot \nabla\frac{\partial \mathbf{u}}{\partial x_0} - C\int_{-\infty}^{t} dt'\left(\frac{d}{dt'}\frac{\partial \mathbf{w}}{\partial x_0} + \frac{\partial \mathbf{w}}{\partial x_0}\right. \\ & \left.\cdot\nabla\mathbf{u} + (\mathbf{w}+\hat{\mathbf{g}})\cdot\nabla\frac{\partial \mathbf{u}}{\partial x_0}\right)(t-t')^{-1/2} - D\mathbf{S} \\ & \times\frac{\partial \mathbf{w}}{\partial x_0} - D\frac{\partial \mathbf{S}}{\partial x_0}\times(\mathbf{w}+\hat{\mathbf{g}}).\end{aligned} \tag{A2}$$

Since this equation requires $\partial\mathbf{S}/\partial x_0$, we obtain an equation for $\partial\mathbf{S}/\partial x_0$ by differentiating (10):

$$\begin{aligned}\frac{d}{dt}\frac{\partial \mathbf{S}}{\partial x_0} = & -\frac{1}{2}\frac{\partial}{\partial x_0}\frac{D\omega}{Dt} - \frac{1}{2}\frac{\partial \mathbf{w}}{\partial x_0}\cdot\nabla\omega - \frac{1}{2}(\mathbf{w}+\hat{\mathbf{g}})\cdot\nabla\frac{\partial\omega}{\partial x_0} \\ & -\frac{10}{3}\frac{\partial \mathbf{S}}{\partial x_0}.\end{aligned} \tag{A3}$$

Replacing ∂x_0 with ∂y_0 gives the equation set that yields $\partial\mathbf{x}/\partial y_0$ for use in (13). Thus, we have nine coupled first-order differential equations for nine vectors. Those equations must be solved simultaneously. For a three-dimensional flow, there are $3\times 9=27$ coupled equations for the nine vectors' components. The initial condition for $\partial\mathbf{x}/\partial x_0$ is unity for the component of $\mathbf{x}$ that is the same Cartesian component as x_0, and is zero otherwise; likewise for the initial condition for $\partial\mathbf{x}/\partial y_0$. The initial condition for $\partial\mathbf{w}/\partial x_0$ is obtained by operating on the initial condition for $\mathbf{w}$, i.e., (12), with $\partial/\partial x_0$; likewise for the initial condition for $\partial\mathbf{w}/\partial y_0$. Since $\mathbf{S}=0$ in the initial plane, the initial condition for $\partial\mathbf{S}/\partial x_0$ is $\partial\mathbf{S}/\partial x_0=0$; also, $\partial\mathbf{S}/\partial y_0=0$. The history integral in (A2) is zero from $t=-\infty$ to $t=t_0$.

[1] O. Vohl, S. K. Mitra, S. C. Wurzler, and H. R. Pruppacher, "A wind tunnel study of the effects of turbulence on the growth of cloud drops by collision and coalescence," J. Atmos. Sci. **56**, 4088 (1999).
[2] A. Khain, M. Ovtchinnikov, M. Pinsky, A. Pokrovsky, and H. Krugliak, "Notes on the state-of-the-art numerical modeling of cloud microphysics," Atmos. Res. **55**, 159 (2000).
[3] R. A. Shaw, "Particle-turbulence interactions in atmospheric clouds," Annu. Rev. Fluid Mech. **35**, 183 (2003).
[4] R. A. Shaw, W. C. Reade, L. R. Collins, and J. Verlinde, "Preferential concentration of cloud droplets by turbulence: Effects of the early evolution of cumulus cloud droplet spectra," J. Atmos. Sci. **55**, 1965 (1998).
[5] R. A. Shaw, "Supersaturation intermittency in turbulent clouds," J. Atmos. Sci. **57**, 3452 (2000).
[6] P. A. Vaillancourt and M. K. Yau, "Review of particle-turbulence interactions and consequences for cloud physics," Bull. Am. Meteorol. Soc. **81**, 286 (2000).
[7] R. R. Rogers and M. K. Yau, *A Short Course in Cloud Physics* (Pergamon, Oxford, 1989).
[8] K. V. Beard and H. T. Ochs, "Warm-rain initiation: An overview of microphysical mechanisms," J. Appl. Meteorol. **32**, 608 (1993).
[9] B. M. Pobanz, J. D. Marwitz, and M. K. Politovich, "Conditions associated with large-drop regions," J. Appl. Meteorol. **33**, 1366 (1994).
[10] R. J. Hill and J. M. Wilczak, "Pressure structure functions and spectra for locally isotropic turbulence," J. Fluid Mech. **296**, 247 (1995).
[11] R. J. Hill and S. T. Thoroddsen, "Experimental evaluation of acceleration

correlations for locally isotropic turbulence," Phys. Rev. E **55**, 1600 (1997).
[12] R. J. Hill, "Scaling of acceleration in locally isotropic turbulence," J. Fluid Mech. **452**, 361 (2002).
[13] A. La Porta, G. A Voth, A. M. Crawford, J. Alexander, and E. Bodenschatz, "Fluid particle accelerations in fully developed turbulence," Nature (London) **409**, 1017 (2001).
[14] G. A Voth, A. La Porta, A. M. Crawford, J. Alexander, and E. Bodenschatz, "Measurement of particle accelerations in fully developed turbulence," J. Fluid Mech. **469**, 121 (2002).
[15] D. Legendre and J. Magnaudet, "A note on the lift force on a spherical bubble or drop in a low-Reynolds-number shear flow," Phys. Fluids **9**, 3572 (1997).
[16] E. E. Michaelides, "Review—The transient equation of motion for particles, bubbles, and droplets," J. Fluids Eng. **119**, 233 (1997).
[17] D. I. Pullin and P. G. Saffman, "Vortex dynamics in turbulence," Annu. Rev. Fluid Mech. **30**, 31 (1998).
[18] H. Mouri, A. Hori, and Y. Kawashima, "Vortex tubes in velocity fields of laboratory isotropic turbulence: Dependence on the Reynolds number," Phys. Rev. E **67**, 016305 (2003).
[19] H. Mouri, A. Hori, and Y. Kawashima, "Vortex tubes in turbulence velocity fields at Reynolds numbers $Re_\lambda \simeq 300$–1300," Phys. Rev. E **70**, 066305 (2004).
[20] S. I. Rubinow and J. B. Keller, "The transverse force on a spinning sphere moving in a viscous fluid," J. Fluid Mech. **11**, 47 (1961).
[21] P. G. Saffman, "The lift on a small sphere in a slow shear flow," J. Fluid Mech. **22**, 385 (1965); corrigendum, *ibid.* **31**, 385 (1965).
[22] J. B. McLaughlin, "Inertial migration of a small sphere in linear shear flows," J. Fluid Mech. **224**, 261 (1991).
[23] K. Miyazaki, D. Bedeaux, and J. B. Avalos, "Drag on a sphere in slow flow," J. Fluid Mech. **296**, 373 (1995).
[24] T. R. Auton, J. C. R. Hunt, and M. Prud'Homme, "The force exerted on a body in inviscid unsteady non-uniform rotational flow," J. Fluid Mech. **197**, 241 (1988).
[25] J. Magnaudet, M. Rivero, and J. Fabre, "Accelerated flows past a rigid sphere or a spherical bubble. Part I. Steady straining flow," J. Fluid Mech. **284**, 97 (1995).
[26] R. Mei, C. J. Lawrence, and R. J. Adrian, "Unsteady drag on a sphere at finite Reynolds number with small fluctuations in the free-stream velocity," J. Fluid Mech. **233**, 613 (1991).
[27] L. D. Landau and E. M. Lifshitz, *Mechanics* (Pergamon, Oxford, 1960).
[28] R. Clift, J. R. Grace, and M. E. Weber, *Bubbles, Drops, and Particles* (Academic, New York, 1978).
[29] V. Armenio and V. Fiorotto, "The importance of the forces acting on particles in turbulent flows," Phys. Fluids **13**, 2437 (2001).
[30] F. Candelier, J. R. Angilella, and M. Souhar, "On the effect of the Boussinesq–Basset force on the radial migration of a Stokes particle in a vortex," Phys. Fluids **16**, 1765 (2004).
[31] M. R. Maxey and J. J. Riley, "Equation of motion for a small rigid sphere in a nonuniform flow," Phys. Fluids **26**, 883 (1983).
[32] C. T. Crowe, T. R. Troutt, and J. N. Chung, "Particle interactions with vortices," in *Fluid Vortices*, edited by S. I. Green (Kluwer Academic, Dordrecht, The Netherlands, 1995), pp. 829–861.
[33] M. J. Manton, "On the motion of a small particle in the atmosphere," Boundary-Layer Meteorol. **6**, 487 (1974).
[34] M. W. Reeks and S. McKee, "The dispersive effects of Basset history integrals on particle motion in a turbulent flow," Phys. Fluids **27**, 1573 (1984).
[35] R. Mei, "Flow due to an oscillating sphere and an expression for unsteady drag on the sphere at finite Reynolds number," J. Fluid Mech. **270**, 133 (1994).
[36] C. J. Lawrence and R. Mei, "Long-time behavior of the drag on a body in impulsive motion," J. Fluid Mech. **283**, 307 (1995).
[37] R. Mei and C. J. Lawrence, "The flow field due to a body in impulsive motion," J. Fluid Mech. **325**, 79 (1996).
[38] P. M. Lovalenti and J. F. Brady, "The temporal behavior of the hydrodynamic force on a body in response to an abrupt change in velocity at small but finite Reynolds number," J. Fluid Mech. **293**, 35 (1995).
[39] I. Kim, S. Elghobashi, and W. A. Sirignano, "On the equation for spherical-particle motion: Effect of Reynolds and acceleration numbers," J. Fluid Mech. **367**, 221 (1998).
[40] D. J. Vojir and E. E. Michaelides, "Effect of the history term on the motion of rigid spheres in a viscous fluid," Int. J. Multiphase Flow **20**, 547 (1994).
[41] O. A. Druzhinin and L. A. Ostrovsky, "The influence of Basset force on particle dynamics in two-dimensional flows," Physica D **76**, 34 (1994).
[42] L. Boltzmann, *Lectures on Gas Theory* (University of California Press, Berkeley, CA, 1964).
[43] D. ter Haar, *Elements of Statistical Mechanics* (Rinehart, New York, 1954).
[44] See EPAPS Document No. E-PHFLE6-17-003503 for an appendix to this paper. A direct link to this document may be found in the online article's HTML reference section. The document may also be reached via the EPAPS homepage (http://www.aip.org/pubservs/epaps.html) or from ftp.aip.org in the directory /epaps/. See the EPAPS homepage for more information.
[45] R. Mei and K. C. Hu, "On the collision rate of small particles in turbulent flow," J. Fluid Mech. **391**, 67 (1999).
[46] S. Sundaram and L. R. Collins, "Collision statistics in an isotropic particle-laden turbulent suspension. Part 1. Direct numerical simulation," J. Fluid Mech. **335**, 75 (1997).
[47] L.-P. Wang, A. S. Wexler, and Y. Zhou, "Statistical mechanical description and modeling of turbulent collision of inertial particles," J. Fluid Mech. **415**, 117 (2000).
[48] P. G. Saffman and J. S. Turner, "On the collision of drops in turbulent clouds," J. Fluid Mech. **11**, 16 (1956).
[49] J. M. Burgers, "A mathematical model illustrating the theory of turbulence," Adv. Appl. Mech. **1**, 171 (1948).
[50] A. Pumir, "A numerical study of pressure fluctuations in three-dimensional, incompressible, homogeneous, isotropic turbulence," Phys. Fluids **6**, 2071 (1994).
[51] B. Marcu, E. Mieburg, and P. K. Newton, "Dynamics of heavy particles in a Burgers vortex," Phys. Fluids **7**, 400 (1995).
[52] J. Davila and J. C. R. Hunt, "Settling of small particles near vortices and in turbulence," J. Fluid Mech. **440**, 117 (2001).
[53] B. Marcu, E. Mieburg, and N. Raju, "The effect of streamwise braid vorticies on the particle dispersion in a plane mixing layer. II. Nonlinear particle dynamics," Phys. Fluids **8**, 734 (1996).
[54] R. J. Hill, "Length scales of acceleration for locally isotropic turbulence," Phys. Rev. Lett. **89**, 174501 (2002).
[55] R. Mei and R. J. Adrian, "Flow past a sphere with an oscillation in the free-stream velocity and unsteady drag at finite Reynolds number," J. Fluid Mech. **237**, 323 (1992).
[56] J. C. H. Fung, "Residence time of inertial particles in a vortex," J. Geophys. Res. **105**, 14261 (2000).
[57] M. J. Manton, "The equation of motion for a small aerosol in a continuum," PAGEOPH **115**, 547 (1977).
[58] S. Kim and S. J. Karrila, *Microhydrodynamics: Principles and Selected Applications* (Butterworth-Heinemann, Boston, 1991).